THE PENNSYLVANIA STATE UNIVERSITY
SCHREYER HONORS COLLEGE

DEPARTMENTS OF ENGINEERING SCIENCE AND MECHANICS AND ASTRONOMY AND ASTROPHYSICS

SENSITIVITY STUDY OF COHERENT MULTI-MESSENGER ASTROPHYSICAL EVENT ANALYSIS

JOSHUA FIXELLE

Fall 2013

A thesis
submitted in partial fulfillment
of the requirements
for baccalaureate degrees
in Engineering Science and Astronomy and Astrophysics
with interdisciplinary honors in Engineering Science and Astronomy and Astrophysics

Reviewed and approved* by the following:

Miles W. Smith
Research Associate
Thesis Supervisor

David J. Miller
Professor of Electrical Engineering
Thesis Supervisor

Christine Masters
Associate Professor of
Engineering Science & Mechanics
Honors Adviser

William N. Brandt
Distinguished Professor of Astronomy
Honors Adviser

Judith A. Todd
P. B. Breneman Chair and Professor of
Engineering Science and Mechanics
Department Chair

Abstract

The concept of multi-messenger event detection has long been explored in the context of above-threshold analysis performed by the IceCube collaboration using Swift BAT and by the Amanda collaboration using BATSE. While these investigations produced null results, they left the event space of sub-threshold events untouched. This untapped event space, combined with the addition of new observatories for various bands and messenger types, provides the obvious niche for a GBN style network to exist: AMON. Important theory and concepts for hypothesis testing and event correlations were developed and brought into the context of multi-messenger astrophysics. Toy models were then developed for relevant neutrino and gamma-ray observatories, along with a model for neutrino-gamma source spectrum via the Guetta model. Monte-Carlo models were considered for pair-wise detection between sub-threshold IceCube neutrino doublets, sub-threshold neutrino-gamma doublets with Swift BAT, and with sub-threshold higher multiplicity neutrino-gamma coincidences with Fermi LAT. Several detection methods were considered and compared to a status quo analyses of neutrino doublets by IceCube, demonstrating a significant sensitivity gain in previously un-excluded parameter space.

Table of Contents

List of Figures

List of Tables

List of Symbols

$\lambda, \hat{x}, \vec{\sigma}$	Event Goodness measure, Event position reconstruction, and event position uncertainty, p. 7
D, D_{th}	Refined Goodness measure with error tolerances considered and an acceptance threshold, p. 7
$P(X), R(X)$	Probability of X and Rate of X (events per unit time), respective, p. 11
ξ_i, Ξ, Λ	The i^{th} event in the event space residing in the total set of all event spaces, respectively, p. 9
$\mathcal{T}_1, \mathcal{T}_0, \mathcal{F}_1, \mathcal{F}_0$	True positive, True negative, False negative, False positive, respectively, p. 11
E_γ, E_ν	Source energy (gamma-ray and neutrino, respectively). For this thesis, we will consider energies in MeV, p. 16
$\Phi(E)$	The differential number flux of a source as seen by the observatory, p. 16
$g(E)$	The spectral shape of the differential number flux as seen by the observatory. This function will be in the form of a broken power law, and is dimensionless, p. 16
$\mathcal{N}, \mathcal{F}$	Number and Energy fluence (per unit area) of a source as measured by the observatory, respectively, p. 16
f_γ, f_ν	spectrum intensity coefficients (gamma-ray and neutrino, respectively), p. 17
$\alpha_\nu, \beta_\nu, \gamma_\nu, \alpha_\gamma, \beta_\gamma$	Spectral slopes for the neutrino and gamma-ray energy spectra, p. 17
$\epsilon_\gamma, \epsilon_{\nu,1}, \epsilon_{\nu,2}$	Break energies for the gamma-ray and neutrino energy spectra, p. 17
R_B, R_S	Background Event and Signal Event rates, p. 18
s_ν, b_ν	Neutrino signal and background event count, respectively, p. 19
B_i, S_i	Background and signal probability distributions for observatory i, respectively, p. 26
A_{total}	Total analysis algorithm acceptance, p. 27

Acknowledgments

I would like to thank professor Derek Fox for his insightful discussions into astrostatistics, the behavior of Swift, the BAT detector, and how to go about analyzing GRB data. I would like to thank professor Douglas Cowen for his insights into the workings of the IceCube observatory, as well as providing financial support for my work on this project. I would like to thank professor Péter Mészáros for his help with compiling a list of multi-messenger sources, and discussion of the physics behind their multi-messenger signal production. I would like to thank professor Jogesh Babu for his discussions on astrostatistics and aid in understanding the statistical difference between coherent and coincident analyses. I would like to thank Andy Youstic for generously providing me with a Linux Box and bulk space in which to develop and run my analysis code, as well as his helpfulness with installing the countless libraries required to complete this task. And finally, I would like to thank my thesis adviser Miles Smith, for his help and support on this project, for this project would not have produced such significant results without his guidance.

Broader Impacts

This thesis focuses on concepts of designing statistical methods for identifying astrophysical signal from false positive coincidences in the context of multi-messenger astrophysics. While this thesis is primarily relevant to the multi-messenger astrophysics and astrostatistics communities, these methods can be applied to much broader problems. Essentially, the methods developed in this thesis can be applied to any problem that requires hypothesis testing under the constraints of false alarm rate and the probability that the input data itself may not be accurate. Other communities in which this topic is relevant include domestic applications for disease or terror alerts, financial fraud detection, and military projectile detection and tracking. One of the simplest examples would be that of disease and terror alerts. Consider a situation where bio detectors are placed around a building, or even a city. Each bio detector has a possibility of producing a false positive alert due to a failure of the detector itself. If several bio detectors produce alerts over a period of time, then a probability of threat can be obtained, as well as a location of the event and its path over time if it is non-stationary (point source or diffusion). The statistical and mathematical tools to deal with such a problem have been previously developed in several different communities and have been summarized and vetted in this thesis.

This thesis involved a substantial engineering component in the aspect of designing statistical analysis methods based on general probability theory, as well as software development. A quick and efficient software framework was developed for performing the Monte Carlo analyses in this thesis, allowing for easy modification and expansion between methods involving very little alteration of the base code. While there exists over three thousand lines of code used for this thesis, the length of unique and independent code is around one thousand lines (the framework), with the other two thousand lines consisting of copied and slightly modified versions of the original framework. Additionally, concepts of algorithm optimization, parallelization of code, and computing speed were implemented in an effort to quickly compute high precision results.

Chapter 1

Introduction

1.1 Multi-Messenger Astrophysics

It is said that the more beautiful a phenomenon in the universe is, the more dangerous it is. It can also be said that these dangerous phenomena are the most interesting, providing valuable insights into the very deep inner workings of the universe itself - physics.

For the standpoint of physics and by consequence, astronomy, the universe is entirely described by the four fundamental forces, each having their own respective messenger and mediator particles: 1) Electro-Magnetic force (photons), 2) Gravitational force (gravitons and gravity waves), 3) Strong force (Gluons and Cosmic rays), and 4) Weak force (Bosons and Neutrinos). Historically speaking, the field of astronomy has focused on information from the electromagnetic force in the form of photons. Further simplified, it has focused on optical astronomy, which has only recently been expanded to include other part of the electromagnetic spectrum such as concurrent radio, infrared, and x-ray observations of sources. Due to the complex interaction of particles and processes in astrophysical events which capture the essence of physics, information from one force and by consequence from one messenger type is not enough. With the advent of new detectors that are capable of detecting and reconstructing cosmic ray showers, neutrino paths, and gravity waves, one can now begin to consider the concept of incorporating information from several different messenger types to obtain a more complete picture of insightful astrophysical phenomena. This idea of incorporating information from multiple fundamental forces is the concept of multi-messenger astrophysics.

Due to the constraint of multiple messenger particles, coupled with the known mechanisms to produce such particles, multi-messenger astrophysics has been limited to three main physical systems: 1) The core collapse model, 2) the merger model, and 3) Blazars and Active Galactic Nuclei (AGN). Each of these models will be discussed in more detail in the following subsections, as well as a few alternate multi-messenger models. Additionally, an important model to consider is that of the Gamma-Ray Burst (GRB). GRBs are expected to result from several of the following

models, however, they deserve special attention as they are the primary focus of this thesis.

1.1.1 Core Collapse

One of the most promising candidates for multi-messenger events would be that of the core collapse model. This model is primarily referring to late stage stellar evolution of massive stars, resulting in either the production of a neutron star or a black hole. As the star begins to age, it goes beyond the stable nucleosynthesis level of converting silicon and sulfur into nickel and iron. At this point, the core ceases burning, and becomes an isothermal core of increasing size, supported by degeneracy pressure. As this isothermal core expands with burning in a thin shell around the core, the outward pressure from the nuclear burning begins to drop, until eventually the gravitational force from the outer layers of the star and core exceed the outward pressure of the core itself. This is identical to the statement of the iron core exceeding the Chandrasekhar mass for an iron core. At this point, the star begins to collapse, causing temperatures to rise, and initiating the rapid neutron capture process (r-process) which begins forming heavier elements, releasing enormous amounts of energy, and therefore resulting in a supernova. What is left over after the supernova will either be a neutron star or a black hole, depending upon the mass of the core before collapse.

Due to the angular momentum of the star, the supernova should be composed of two components: 1) an isotropic expansion of the star, and 2) polar plasma jets along the axis of rotation. It is possible for the isotropic expansion component to overtake the polar plasma jets which can cause the plasma jets to stall and become trapped within the supernova remnant. It is theorized that these plasma jets are a primary source for high luminosity GRBs. In either case, shock waves are produced within the plasma (either in the jets or in the isotropic remnant), resulting in the Fermi-acceleration of protons enabling $p - \gamma$ interactions to produce neutrinos. Additionally, these events should produce large numbers of cosmic rays (highly energetic protons) which could potentially be detected at Earth, along with their photon and neutrino counterparts. Due to the isotropic collapse of the star, it is unlikely that such an event will produce gravity waves.

In general, the supernova model is used to describe a core collapse, most likely forming a resultant neutron star. There also exists a class of highly energetic supernova called hypernova resulting in the formation of a black hole. Rough estimates suggest that hypernovas represent somewhere between 1-3% of the supernova population. There also exists a classification of prolonged supernova called supranova, which occur when a core collapse produces a neutron star, and then later collapses into a black hole in a time period ranging from days to months. The supranova population is expected to make up a very small fraction of the overall supernova population [1].

Typical supernova neutrino production energies are expected to be on the order of 10^{13} GeV with hypernova neutrino production energies on the order of 10^{17} GeV. Furthermore, one can expect the neutrino and photon luminosities of the hypernova to be on order of 10-100 times greater than that of the respective supernova luminosities. One can also estimate the event

rate of supernovae in the Galaxy to be on order of one per every 30-50 years, with hypernova consisting of 1-3% of this population. If the estimate were to be expanded to a 20 Mpc range, one can expect the rate of hypernovae to be around one per year with energies of neutrinos that Icecube could detect (Icecube could not detect extra-galactic supernovae) [2, 3, 4].

1.1.2 Mergers

Another promising candidate for multi-messenger events is that of neutron star - neutron star and neutron star - black hole mergers. In this situation, the two compact objects form a binary system which begins to slowly radiate gravitationally, causing the system to loose energy. As the energy is lost, the orbital radius decreases, angular momentum is conserved, and the velocity increases. Eventually the orbital radius has decreased to the point where the two compact objects collide, resulting in a merger event. Such an event could be a source for short, hard spectrum GRBs. If that is the case, one should expect that a merger would produce all four messenger types in the form of photons, neutrinos from $p-\gamma$ interactions in the resultant GRB, cosmic rays from the GRB, and gravity waves.

In the case of double mergers, one can expect shockwaves from the merger to act as short GRBs known as kilanova. These GRBs should primarily produce photons and strong gravitational wave radiation, with the potential for a weak neutrino detection. These mergers are estimated to occur at a rate of approximately one per million years per galaxy. To counter this low event rate, one can expect the resultant radiation to be detectable up to a red shift of $Z \sim 1$ [5, 6, 7, 8].

1.1.3 Blazars and Active Galactic Nuclei

Another possible model is that of the active galactic nucleus (AGN), where a super massive black hole at the center of a galaxy is accreting matter and ejecting plasma jets along its axis of rotation. A Blazar is a special form of AGN which is very compact and exists typically at high red shifts, in which the relativistic plasma jets are beamed towards Earth. These phenomena are often observed at many wavelengths, most notably in radio bands. While current observations show the existence of AGN and Blazars with photon emissions, they should also have neutrino production in their jets due to the $p-\gamma$ interactions in the resultant shocks. Due to their distance, however, low neutrino luminosities are expected. Additionally, non-jet AGNs which are considered "radio quiet" may produce higher luminosity neutrinos due to shocks in the accretion disk. The symmetry of these events predicts that no gravitational wave radiation would be produced [9, 10].

1.1.4 Alternate Multi-Messenger Models

There are a few other multi-messenger source models that exist with less popularity than the aforementioned three. These are: 1) Primordial Black Holes, and 2) Cosmogenic Neutrinos.

Primordial black holes are black holes that were formed from density perturbations shortly after the Universe stabilized proceeding the Big Bang. While there are theorized to have been many different masses of black holes produced, many have already evaporated away via Hawking Radiation. Theory predicts that there may be a small population of primordial black holes that should be evaporating at present time, which may produce neutrinos and photons at the moment that the black hole completely dissipates [11, 12, 13]. The cosmogenic neutrinos are expected to occur from stray cosmic rays interacting in the interstellar medium. The high energy protons or nucleons exhibit extinction by infrared and Cosmic Microwave Background (CMB) photons, allowing for possible $p - \gamma$ interactions, therefore producing neutrinos. These neutrinos should arrive at earth along with other particles from the incident cosmic ray [14]. This would be a prime example of a multi-messenger event that does not include a photon component (cosmic rays and neutrinos only).

1.1.5 Gamma-Ray Bursts

The standard model for GRBs is that of the relativistic fireball. The model assumes that plasma is being beamed in a relativistic jet with speed represented by a bulk Lorentz factor Γ. Within this beamed jet, high energy protons interact with photons to produce neutrinos via the Δ resonance and then later pion decay (i.e. $p - \gamma$ interaction). The resonance is given by:

$$p + \gamma \rightarrow \Delta^{+} \rightarrow n + \pi^{+}$$

where p is a proton, γ is a photon, Δ^{+} is a delta baryon, n is a neutron, and π^{+} is a pion. The pions then follow a decay chain as follows:

$$\begin{aligned} \pi^{+} &\rightarrow \mu^{+} + \nu_{\mu} \\ \mu^{+} &\rightarrow e^{+} + \nu_{e} + \bar{\nu}_{\mu} \end{aligned}$$

where μ^{+} is an anti-muon, ν_{μ} is a muon neutrino, e^{+} is a positron, ν_{e} is an electron neutrino, and $\bar{\nu}_{\mu}$ is an anti-muon neutrino. This model predicts large amounts of ν_{μ} and ν_{e} to be produced, both of which a neutrino detector such as Icecube can detect [15]. It should be recalled that there exists a resonance between the three neutrino flavors, where we expect some of the neutrino flux to be converted into tau neutrinos ν_{τ} by the time it reaches Icecube. This model serves as the motivation for the later mentioned Guetta model [16]. Constraints have been placed on a coupled parameter space of bulk Lorentz factor Γ and the ratio of neutrinos to photons in the jet [15].

1.2 The Concept of AMON

To obtain a more complete understanding of these violent phenomena, one must expand the present detection capabilities beyond that of the status quo detection of photons to that

of other messenger types. The standard model consists of four fundamental forces: 1) Electro-Magnetic force (photons), 2) Gravitational force (gravitons and gravity waves), 3) The Strong force (Gluons and Cosmic rays), and 4) the Weak force (Bosons and Neutrinos). As per the status quo method of detecting these violent phenomena, only one messenger type (specifically photons) is considered. However, as per the results of several physical models [16], one should expect to see the event energy distributed among the four messenger types. This distribution of event energy over the four messenger types can be leveraged in terms of increasing the signal to noise of an overall detection (i.e. the increased ability to detect a faint source) as well as the added benefit of constraining physical models and parameters based on detections (or lack there of). This leveraging of the four messenger types to detect these interesting and insightful phenomena, by the collaboration of many observatories throughout the globe is the concept of multi-messenger astrophysics.

In basic detection theory, one typically considers the signal to noise characteristic of a detector, which represents the level of signal to that of the background noise. Since many interesting physical phenomena are more likely to occur at large distance from Earth, the expected level of signal will be sufficiently small, and is often buried in the noise. A common technique for increasing this value in the background dominated regime, is to combine data from multiple observing runs, with the implicit assumption that the source is varying slowly. The expected improvement of signal to noise should vary as $\sqrt{n}$, where n is the number of data sets combined. Unfortunately, for quick sources such as violent astrophysical phenomena, often leading to gamma-ray bursts, one does not have the luxury of multiple observing runs. To solve this problem, many different observatories must be used to coherently detect the source, increasing the signal to noise by approximately $\sqrt{n}$, where n is the number of observatories. The majority of these weak signals will also occur at a level that is below an instrument set threshold making the individual observatory events "sub-threshold". Therefore, by developing a way to compile large amounts of sub-threshold data from various observatories in real time, a significant increase the detection sensitivity of faint, short lived sources can be achieved.

This idea has been tested several times in recent years between the Antarctic Muon And Neutrino Detector Array (AMANDA) group (neutrinos) in collaboration with the Burst and Transient Source Experiment (BATSE) instrument on the Compton Gamma Ray Observatory (CGRO) (x-rays) [16, 17]. Additionally, this method has been attempted by the IceCube collaboration and the Swift telescope (using the Burst Alert Telescope instrument)[18]. All precursor analyses have been primarily focused on above-threshold events, and therefore lost significant sensitivity to parameter space. With the advancement of instrumentation (e.g. the IceCube 86 string experiment and the Fermi Large Area Telescope instrument), as well as combing sub-threshold data, one can significantly improve parameter space sensitivity.

Another challenge of performing real time event detection will be following up alerts. If some multi-observatory network is successful at identifying an event, it must alert a series of followup observatories quickly, in an effort to capture the afterglow of the event before it disappears (to obtain more detailed spectral information). A similar network currently exists in the case of

GRB followup called the Gamma Ray Burst Network (GBN), providing a paradigm that could act as a predecessor of a more complex network of multi-channel correlation and analysis. This multi-messenger, multi-channel network proposition is to be known as the Astrophysical Multi-Messenger Observatory Network (AMON) [19].

1.3 A Preview of Things to Come

This thesis will discuss the research conducted in regards to developing and applying statistical analyses and hypothesis testing for multi-messenger event correlation. The thesis will focus on the detection of GRBs using a single neutrino triggering event, followed by temporal coincidence with a secondary sub-threshold messenger (e.g. another neutrino, or photon data). The second chapter describes a way to think about the analysis that is being posed from the perspective of functional analysis, as well as some basic definition and primers to hypothesis testing, the Log-Likelihood analysis, Receiver Operating Characteristic Curves, and the difference between Coincidence and Coherent event analysis. The third chapter discusses the broken power law spectral models for the neutrino and photon spectrum that are considered for the GRBs in question, along with their connection through the Guetta model. The third chapter also discusses the three observatories of interest (IceCube, Fermi LAT, and Swift BAT), and outlines a "toy" model for each. The fourth chapter presents results for the three pairings considered (IC-IC, IC-BAT, and IC-LAT), building upon another and increasing complexity as the chapter progresses. Additionally, chapter four outlines a way to implement further result rejection which is tailored towards the followup observatory. The fifth chapter begins with a way to combine all of the results from chapter four, and provide some final culminating result of the thesis - analysis gain. Chapter five then concludes with a proposal for future work to be conducted as a followup to this thesis.

Chapter 2

Analysis Algorithms

2.1 The General Algorithm

The goal of the general analysis algorithm is to take incoming event data from several sources, whether it be individual events such as a single photon or packaged events such as an influx of photons, and produce some estimate of "Statistical Goodness" for detection of a source as well as a localized detection location from the analyzed events. To better understand this, one can consider looking at a mathematical definition in terms of functional analysis and set theory.

To develop this theory, we assume the existence of three vector spaces $S \in \mathbb{R}^\ell$, $O \in \mathbb{R}^n$, and $A \in \mathbb{R}^m$, corresponding to the space of all sources, observatory information, and the analysis, respectively. It should be noted that the dimensional constraints on the above spaces are such that $\ell \geq n \geq m$, where the goal of any analysis it to take the data from the O space and reduce it to a low dimensional surface in A. In principle, S is an infinite dimensional Hilbert space, and O consists of a finite dimensional Hilbert space that provides an "approximation" to S. This approximation is done through a functional mapping $\mathcal{T}$ (the telescope function) given by:

$$\mathcal{T} : S \mapsto O,\ S \in \mathbb{R}^\ell,\ O \in \mathbb{R}^n$$

where $\mathcal{T}$ encompass both the universe acting on the source space (e.g. attenuation due to extinction, etc.) as well as the physics of the specific observatories that are detecting the source.

To illustrate this, consider a black body radiating, where the photon energy emitted can be represented by the black body distribution function $B(\nu, T)$, which is indeed a Hilbert function (assuming infinitesimal discretization in ν). Here, the black body distribution function behaves as a surface in S parameterized by the temperature of the black body T. Now, let there be two observatories, $O_1 \subset O$ and $O_2 \subseteq O$. The observatory O_1 is equipped with two filters, with fluxes f_B (455 nm) and f_V (551 nm), while the observatory O_2 is equipped with four filters, with fluxes f_B, f_V, f_Z (900 nm), and f_K (2190 nm). If both observatories scan the

sky, sampling the source space S, their individual sensitivities to model parameter space[1] are comparable at high temperatures, however, the sensitivity of O_2 is much more sensitive at lower temperatures. Furthermore, if one were to attempt to find the temperature parameter T of a source, observatory O_2 will be much better at doing so. In this example[2], the source space has $\ell = \infty$, and the combined observatory space is $n = 4$. We can then define some analysis that either does a model fit for the filter fluxes, or does a simple calculation of $f_B - f_V$ (a typical measure for stars in astronomy), allowing for $m = 1$. In this example, $< O_1, O_2 > \neq 0$, since they both share flux measurements at f_B and f_V. If observatory O_2 were to be reduced to having only sensitivity to f_Z and f_K, then they would have completely unique sensitives to parameter space T with $< O_1, O_2 >= 0$.

Therefore, the analysis algorithm which reduces $O \in \mathbb{R}^n$ to $A \in \mathbb{R}^m$ can be thought of as function f which creates a map from the observatory space of dimension n to the analysis space of dimension m.

$$f : O \mapsto A,\ O \in \mathbb{R}^n,\ A \in \mathbb{R}^m$$

In reality, the analysis algorithm will be looking at some event space Ξ which has a series of event ξ_i and will map these events in the event space into the analysis space. Furthermore, the event space Ξ is actually a subset of a larger domain containing all possible event spaces Λ. For the purpose of this thesis, several different subsets of Ξ will be considered throughout Λ to attempt to obtain a good estimation to how the analysis algorithm will behave on real data. A visual representation of this idea is presented in terms of an n dimensional manifold mapping to an m dimensional space as can seen in Fig.2.1. In the optical observatory examples, the individual filter fluxes would correspond to events ξ_i, where as the ensemble of filter fluxes would compose Ξ. As the temperature parameter T is varied, the event space Ξ would move through Λ, producing different events ξ_i. It should further be noted that the event space Ξ and the events themselves ξ_i are not clearly defined hyper-volumes, but exist as a distribution function which in many cases extends to $\pm\infty$.

The analysis space that was chosen consists of two parameters for a set of events, λ and $\hat{x}$ which represent the "likelihood" that there is a common event and the reconstructed position, respectively. Additionally, a parameter $\vec{\sigma}$ can be obtained to provide an uncertainty in the reconstructed position.

The final goal of the analysis is to redirect significant events for followup observation. Different tolerances for what is considered acceptable position error and false alarm rate will depend on individual followup observatories, which may include allocatable telescope pointing and the field of view of each followup observatory. With that said, it will be useful to define another parameter D which represents a refined value of λ taking followup limitations and tolerances into consideration. Additionally, for analysis acceptance a threshold value D_{th} should be defined, where any grouping of events yielding a value above D_{th} are accepted, and any below are rejected.

[1] In this case there is one parameter - T - assuming all sources are at the same distance and luminosity.
[2] Ignoring positioning and pointing

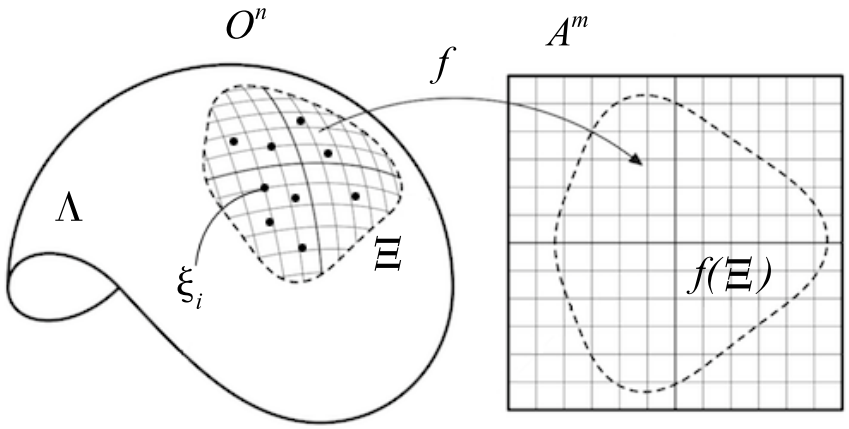

Figure 2.1: A visualization of the global event space Λ as a manifold with the subset event space Ξ containing individual events ξ_i. The visualization also depicts the mapping of the algorithm f from O^n to A^m.

To further illustrate the difference between λ and D, consider two follow up observatories A and B, and an event space Ξ. For the given event space, the analysis algorithm is applied, producing a values of λ. This value of λ is independent of any followup information, it can be a large value (likely to be an event of interest) and have a large uncertainty in position reconstruction, or it can be a moderate value with a small uncertainty in position reconstruction, or anything between. Let observatory A have a field of view of 0.1 steradian and accept 10 false alarms per year. And let observatory B have a field of view of 0.01 steradian and accept 1 false alarm per decade. Now let the result of the analysis algorithm produce a false alarm probability of around three per decade, with a position uncertainty of 0.05 steradian. Obviously this event would not be sent to observatory B, however, it could be sent to observatory A. When the value of D is calculate for observatories A and B, D_A and D_B, respectively, the value of $D_A > D_{A,th}$ and $D_B < D_{B,th}$ will be found. This is due to the fact that the calculation of D will take the values of λ, $\hat{x}$, and $\vec{\sigma}$, and map them into values of D_A and D_B for the two observatories, taking into account the allowed false alarms for each observatory and their respective field of views.

2.2 The Likelihood Analysis Approach

One way to formulate an analysis is to preform a hypothesis test on the event data, and ask the question "By how much does the current event data differ from what would be expected of a null hypothesis, and what set of parameters maximize the difference?" To answer the first question, a log-likelihood ratio test (2.1) can be used.

$$\lambda = -2 \ln \left[\frac{\mathcal{L}(\mathcal{H}_0|\Xi)}{\mathcal{L}(\mathcal{H}_1|\Xi)} \right] \tag{2.1}$$

Where $\mathcal{H}_0$ is the null hypothesis, $\mathcal{H}_1$ is the alternate hypothesis, and Ξ is the observatory event space. Here the likelihood function $\mathcal{L}(\mathcal{H}_i|\Xi)$ is is given by (2.2). In the case of analyzing two event streams (A and B where the question as to whether or not the two event streams are correlated is being asked) there are three additional hypothesis that must be considered (see Tab. 2.1) besides the null and alternate hypothesis. For more event streams added, this number of possible hypothesis can grow substantially, however, this thesis will only consider the case of two event streams.

$$\mathcal{L}(\mathcal{H}|\Xi) = \prod_{i=0}^{N} P_i(\xi_i|\mathcal{H}), \quad \xi_i \in \Xi \tag{2.2}$$

Where $P_i(\xi|\mathcal{H})$ is a statistically independent probability function for the i^{th} event ξ_i in the event space Ξ containing N events. In general, the probability function P_i should depend upon the specific event data ξ_i. For example, if ξ_n is neutrino data and ξ_{n+1} is photon data, then P_n will be chosen to handle neutrino data and P_{n+1} to handle photon data.

Hypothesis	Description
$\mathcal{H}_0$	Neither A nor B sees signal
$\mathcal{H}_1$	Both A and B see the same signal
$\mathcal{H}_0'$	Both A and B see different signal
$\mathcal{H}_0''$	A sees signal and B sees background
$\mathcal{H}_0'''$	A sees background and B sees signal

Table 2.1: Table showing the possibly hypothesis for two event streams A and B, where the test is for both A and B seeing the same signal. Any other possible situation is not of interest here and is therefore assigned $\mathcal{H}_0$.

Since the log-likelihood ratio produces a value of $\lambda = 0$ for $\mathcal{H}_1 = \mathcal{H}_0$ and a positive value of λ for $\mathcal{H}_1 \neq \mathcal{H}_0$, then the second question posted can be answered by attempting to maximize the log-likelihood function to fit the hypothesis $\mathcal{H}_1$.

2.3 Event Clustering and Selection

Due to a potentially large span of the event space Ξ pre-selection and event clustering may need to be used to aid in improving the computation time of preforming the analysis. One obvious example of why event clustering is needed comes from the possibilities of multi-modal solutions in a minimization based analysis algorithm (e.g. Likelihood analysis). If all possible events are taken, there may be several solution to the analysis, each having their own unique value of λ and $\vec{\sigma}$, therefore the possibility of multiple solutions must be reduced. If the events are pre-cut to a small enough sample, the possibility of multi-modal solutions will be reduced and will most likely result in there being only one unique solution.

One simple method that can be used for quick data selection could be a position cut. Assume that observatory A is a triggering observatory (with a low event rate) with an azimuthaly

symmetric Point Spread Function (PSF) and observatory B is an observatory to be correlated with (with a high event rate) which also has a radially symmetric Point Spread Function. A hard cutoff can be made on the PSF at some tolerance (e.g. 5σ), where the angular distance to this tolerance of the events from an observatory is ψ_i (for $i = 1, \ldots, n$). A position threshold given by $\psi_0 = \max\{\psi_1, \ldots, \psi_n\}$ can then be set, as well as a triggering observatory chosen which emits events j (for $j = 1, \ldots, n$). Then the angular difference between event i and j can be given by ψ_{ij} allowing any event i that satisfies $|\psi_{ij}| > \psi_0$ to be culled.

Another selection method includes creating a temporal cut, where the simplest cut would be a hard cut within a time range of ΔT. Consider a triggering event (i.e. a neutrino detection) that occurs at time t_0. If the goal is to detect a gamma ray burst in coincident with a neutrino, then a temporal cut of $\Delta T > \langle t_{90} \rangle$ can be used, where t_{90} is an intrinsic property describing the burst duration. The remaining question is in regards to how should the time frame ΔT be positioned about t_0. A simple solution would be to straddle the time frame about t_0 leading to a time bracket of $[t_0 - \Delta T/2, t_0 + \Delta T/2]$, or perhaps event extend the range to $[t_0 - \Delta t, t_0 + \Delta T]$ if the value of ΔT is relatively small compared to the expected time between background events of observatories A and B. With that said, any event from observatory B that is outside of the chosen time bracket is culled.

2.4 The ROC Curve

One way of characterizing the effectiveness of a detection algorithm (or a hardware detector for that matter) is to use a Receiver Operating Characteristic curve (ROC curve), which was originally developed for analyzing radar signals during World War II [20]. The ROC curve is a way of visualizing the changing confusion matrix (See Tab. 2.2) for different rejection thresholds in a detection algorithm.

		Actual Value	
		True	False
Predicted Value	True	True Positive ($\mathcal{T}_1$)	False Positive ($\mathcal{F}_0$)
	False	False Negative ($\mathcal{F}_1$)	True Negative ($\mathcal{T}_0$)

Table 2.2: Table depicting the four possible situations of rejection and acceptance for a hypothesis testing algorithm. Each case is shown in more detail in (2.3).

Essentially, each of the values in the confusion matrix can be thought of as the following:

$$\begin{aligned} P(D > D_{th}|\mathcal{H}_1) &= P(\mathcal{T}_1) \\ P(D < D_{th}|\mathcal{H}_1) &= P(\mathcal{F}_1) \\ P(D > D_{th}|\mathcal{H}_0) &= P(\mathcal{F}_0) \\ P(D < D_{th}|\mathcal{H}_0) &= P(\mathcal{T}_0) \end{aligned} \tag{2.3}$$

Essentially, the curve can be parameterized by a value D, where each value of D will yield a

corresponding $P(\mathcal{T}_1)$, $P(\mathcal{T}_0)$, $P(\mathcal{F}_1)$, and $P(\mathcal{F}_0)$. Since the $P(\mathcal{F}_1) = 1 - P(\mathcal{T}_1)$ and $P(\mathcal{T}_0) = 1 - P(\mathcal{F}_0)$, it is sufficient to only plot $P(\mathcal{T}_1)$ against $P(\mathcal{F}_0)$ to represent all four quantities. By doing so, a curve similar to Fig. 2.2 can be obtained. It is important to note that the curve $P(\mathcal{T}_1) = P(\mathcal{F}_0)$ represents the worst possible case for a detection algorithm (corresponding to random guessing), where every ROC curve should remain above this random guessing curve.

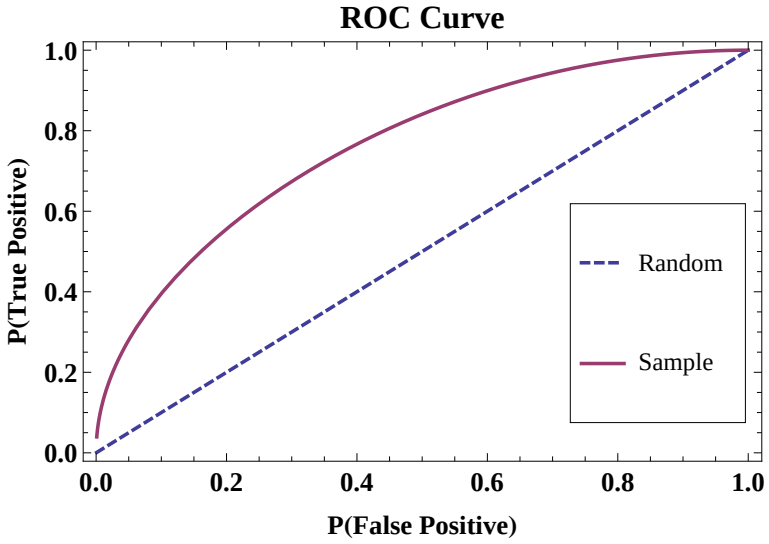

Figure 2.2: Plot of an example ROC curve (purple,thick) and the random guessing line (blue,dashed). The random guessing line represents the curve corresponding to an assignment of $\mathcal{H}_0$ or $\mathcal{H}_1$ randomly for each set of events considered (i.e. the worst possible analysis).

To generate the values of $P(\mathcal{T}_1)$ and $P(\mathcal{F}_0)$ a distribution in D for the null hypothesis $\mathcal{H}_0$ is generated. Then for a specific event space Ξ, a distribution of the resultant analysis algorithm for the alternative hypothesis test $\mathcal{H}_1$ is generated in D. The combined curves looking at the normalized probability above and below some threshold value D_{th} will produce values of $P(\mathcal{T}_1)$ and $P(\mathcal{F}_1)$ as a function of the parameter D_{th} (See Fig.2.3), generating a ROC curve for the event space Ξ. Ideally, a value of D_{th} should be set for the final analysis, which yields acceptable values of $P(\mathcal{T}_1)$ and $P(\mathcal{F}_1)$ based on given analysis tolerances. For the analysis considered in this thesis, suppose for a single observatory there is a background rate of R_B (events per unit time) which correspond to $\mathcal{T}_0$ and a followup observatory which the events are being sent to will accept a false alarm rate of $R(\mathcal{F}_1)$ (events per unit time). Then the highest value of $P(\mathcal{F}_1)$ would roughly correspond to $R(\mathcal{F}_1) \approx R_B P(\mathcal{F}_1)$, which can then be inverted to correspond to a specific value of D_{th} on the ROC curve.

If the event space Ξ is a subset of a larger domain Λ which is to be considered by the analysis, then a useful way to visualize the effectiveness of the analysis algorithm is to consider plotting the values of $P(\mathcal{T}_1)$ as a function of the larger domain Λ for a given value of $P(\mathcal{F}_0)$. This can

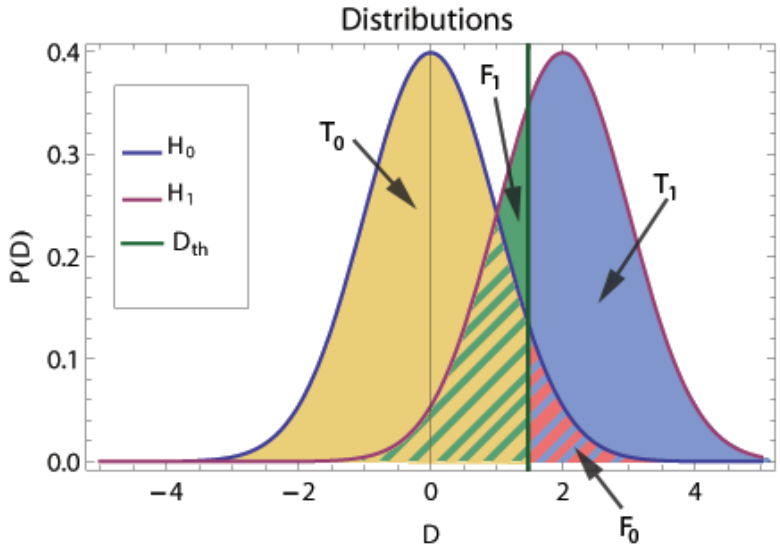

Figure 2.3: Plot of a $\mathcal{H}_0$ and $\mathcal{H}_1$ distribution for a set of events, showing the regions in which correspond to the confusion matrix parameters. The threshold line chosen D_{th} is shown (green,solid) to mark the above acceptance and below rejection on the two distributions.

be done by formulating a generalized null distribution for the algorithm consistent with the $\mathcal{H}_0$ hypothesis to establish an estimate for an acceptable value of D_{th}. Then as the event space Ξ is moved around the domain Λ values of $P(\mathcal{T}_1)$ can be calculated by evaluating the ROC curve at the location $D = D_{th}$ chosen by the $\mathcal{H}_0$ distribution. An example of this would be a simple parameter space that consists of two variables of interest α and β. Each coordinate (α, β) describes an event space Ξ_i containing a number of events $\xi_{i,j}$. The analysis algorithm can then be run for several combinations of (α, β) and be visualized using a contour plot to show the analysis algorithm's effectiveness as a function of the different coordinates of (α, β).

2.5 Coherent vs. Coincident Analysis

When dealing with a series of possible events, the question that one wants to ask is: Are these events related? Given the possible aforementioned hypotheses, this equates to posing the following Bayesian statistics question for n events:

$$\lambda = P(\mathcal{H}_1|\xi_1, \xi_2, \ldots, \xi_n) \tag{2.4}$$

where λ is a measure of statistical "goodness", and ξ_i are individual events. Due to complexity (both computationally and in correctly posing the formulation of P) of performing such an analysis on a series of n events, one often considers the case of coincidence analysis. The coincidence analysis question can be formed by considering the lesser informed cousin of the coherent

analysis: the spatial analysis. Essentially, this coincidence analysis asks the following question between two events:

$$\lambda = P(\mathcal{H}_1|\xi_1, \xi_2) \tag{2.5}$$

where this question is often easily posed, and can be computed analytically or near constant time $O(1)$. The tricky part comes in when considering n events. To do so, one can formulate the following variation to the above as:

$$\begin{aligned} y_1 &= P(\mathcal{H}_1|\xi_1, \xi_2) \\ y_2 &= P(\mathcal{H}_1|y_1, \xi_3) \\ \vdots &\quad \vdots \\ \lambda &= P(\mathcal{H}_1|y_{n-1}, \xi_n) \end{aligned} \tag{2.6}$$

where y_i is the intermediate "goodness" value. Clearly it can be seen that this method poses additional complications, such as statistical equivalence based on ordering. One can also consider the difference between the two analyses graphically in terms of combinatorics. This can be illustrated in Figure2.4.

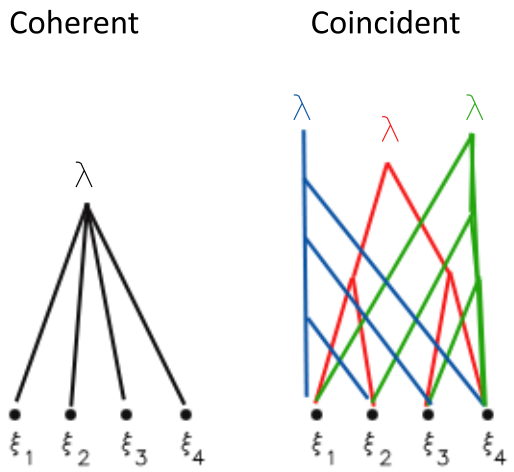

Figure 2.4: Diagram showing the combinatorics difference between the Coherent and Coincidence analyses in terms of pairing. It should be noted that in the case of Coherence, there is only one value of λ, while for Coincidence there are several different values of λ. Note that not all combinations are shown for the Coincidence case.

As it turns out, the two types of analyses are completely different questions, which merge to become the same under the following two conditions: 1) the multiplicity of events is 2 (i.e.

$n = 2$), or 2) all of the probability distributions in question are independent and Gaussian (i.e. $P_i(\mathcal{H}_1|\xi_i)$ is a normal distribution with σ_i). Since the signal to noise of a the overall analysis will grow approximately as $\sqrt{N}$, where N is the number of observatories (assume at least one event per observatory), the former constraint must be relaxed. Additionally, since most of the independent probability distributions will not be Gaussian, the latter constraint must also be relaxed. Because of these two issues, however, this thesis will strictly consider the case of pair wise events (reducing to a coincident analysis, See IC-IC, IC-BAT), or a grouping of events in a coherent analysis (See IC-LAT).

Chapter 3

The Neutrino - Gamma model

After the brief detour into detection theory from the previous chapter, a more quantitative description of the source and observatory models considered will be discussed. It should be noted that all of the following models are assuming Gamma Ray Bursts as the primary event, consisting of neutrino and x-ray flux components.

3.1 A Source Model

Typically in high energy astrophysics, the source spectrum received by the observatory is represented as a function of energy (referred to as the energy spectrum) and is expressed as per energy, as opposed to per hertz as in other types of astronomy. In general the energy spectrum will take a form as follows:

$$\Phi(E) \equiv \frac{dN}{dEdAdt} \equiv fg(E) \tag{3.1}$$

where $g(E)$ is a unit-less broken power law, and f is an amplitude factor. Additionally, a concept of number fluence $\mathcal{N}$ and energy fluence $\mathcal{F}$ are often used to denote the total energy flux and the total number flux over a detector area dA within a given energy band.

$$\mathcal{N} \equiv \int_{E_1}^{E_2} \Phi(E) dEdt \tag{3.2}$$

$$\mathcal{F} \equiv \int_{E_1}^{E_2} \Phi(E) EdEdt \tag{3.3}$$

3.1.1 Neutrino Source

The neutrino source model proposed in [16] and in [18] which uses a broken power law with two energy breaks. Here they define the spectral function $g_\nu(E_\nu)$ as:

$$g_\nu(E_\nu) = \begin{cases} \left(\frac{E_\nu}{\epsilon_{\nu,1}}\right)^{-\alpha_\nu}, & E_\nu < \epsilon_{\nu,1} \\ \left(\frac{E_\nu}{\epsilon_{\nu,1}}\right)^{-\beta_\nu}, & \epsilon_{\nu,1} \leq E_\nu < \epsilon_{\nu,2} \\ \left(\frac{\epsilon_{\nu,2}}{\epsilon_{\nu,1}}\right)^{-\beta_\nu} \cdot \left(\frac{E_\nu}{\epsilon_{\nu,1}}\right)^{-\gamma_\nu}, & \epsilon_{\nu,2} \leq E_\nu \end{cases} \tag{3.4}$$

And the energy spectrum $\Phi_\nu(E_\nu)$ is given by:

$$\Phi_\nu(E_\nu) = f_\nu g_\nu(E_\nu) \tag{3.5}$$

For simplifications, the assumption that the first break energy $\epsilon_{\nu,1}$ is less than the detector energy threshold, and that the second break energy $\epsilon_{\nu,2}$ is much larger than the detector energy threshold, which will allow the spectral shape to be simplified to a simple power law given by:

$$g_\nu(E_\nu) = \left(\frac{E_\nu}{\epsilon_{\nu,1}}\right)^{-\beta_\nu} \tag{3.6}$$

This assumption was made in modeling the source spectrum at the neutrino observatory as it further simplifies the model. Furthermore, the background atmospheric neutrino threshold can be modeled by a single power law following (3.6) with a spectral index of $\beta_\nu = 3.4$ [21, 22].

3.1.2 Gamma-Ray Source

The gamma source model follows a similar pattern to that of the neutrino source model as proposed in [18], which uses a broken power law with only one energy break. The spectral function $g_\gamma(E_\gamma)$ is then defined as:

$$g_\gamma(E_\gamma) = \begin{cases} \left(\frac{E_\gamma}{\epsilon_\gamma}\right)^{-\alpha_\gamma}, & E_\gamma < \epsilon_\gamma \\ \left(\frac{E_\gamma}{\epsilon_\gamma}\right)^{-\beta_\gamma}, & \epsilon_\gamma \leq E_\gamma \end{cases} \tag{3.7}$$

And similarly, the energy spectrum $\Phi_\gamma(E_\gamma)$ is given by:

$$\Phi_\gamma(E_\gamma) = f_\gamma g_\gamma(E_\gamma) \tag{3.8}$$

Furthermore, the background gamma-ray spectrum can be modeled by a single power law with a spectral index of $\beta_\gamma = 2.4$ [23].

3.1.3 The Guetta Model

A connection between the gamma source model and the neutrino model was proposed in [16], and was refined further in [18]. Here the spectral indices, break energies, and amplitude factors were correlated. The indices follow: $\alpha_\nu = 3 - \beta_\gamma$, $\beta_\nu = 3 - \alpha_\gamma$, and $\gamma_\nu = \beta_\nu + 2$. The two energy breaks were correlated as follows:

$$\begin{aligned} \epsilon_{1,\nu} &= 7 \cdot 10^5 \text{ GeV } \frac{1}{(1+z)^2} \left(\frac{\Gamma_{\text{jet}}}{10^{2.5}}\right)^2 \left(\frac{\text{MeV}}{\epsilon_\gamma}\right) \\ \epsilon_{2,\nu} &= 10^7 \text{ GeV } \frac{1}{1+z} \sqrt{\frac{\epsilon_e}{\epsilon_B}} \left(\frac{\Gamma_{\text{jet}}}{10^{2.5}}\right)^4 \left(\frac{t_{\text{var}}}{0.01 \text{ s}}\right) \sqrt{\frac{10^{52} \text{ erg s}^{-1}}{L_\gamma^{\text{iso}}}} \end{aligned} \tag{3.9}$$

where z is the red shift of the GRB, ϵ_e is the fraction of energy in electrons, ϵ_B is the fraction of energy in magnetic field, t_{var} is the time variability of the gamma ray light curve, Γ_{jet} is the lorentz boost factor of the jet, and L_γ^{iso} is the isotropic luminosity of the GRB. The amplitude factors are defined as follows:

$$\int_0^\infty \left(\frac{d\mathcal{F}_\nu}{dE\nu}\right) dE_\nu = \frac{1}{8}\frac{1}{f_e}(1 - (1 - \langle x_{p\to\pi}\rangle)^{\Delta R/\lambda_{py}}) \int_{1 \text{ KeV}}^{10 \text{ MeV}} \left(\frac{d\mathcal{F}_\gamma}{dE\gamma}\right) dE_\gamma \tag{3.10}$$

where f_e is the ratio of energy between electrons and photons, $\langle x_{p\to\pi}\rangle$ is the average fraction of energy going from protons to pions, λ_{py} is the mean free path of the jet, and ΔR is the approximate size of the shock. It should be noted that most of these parameters are well constrained (or of order unity) with regard to Γ_{jet} [16]. The IceCube 40 experiment has ruled out possible values of Γ_{jet} below $\Gamma_{\text{jet}} \approx 360$, and the IceCube 86 experiment will be able to improve the limit to rule out values below $\Gamma_{\text{jet}} \approx 490$ [15].

3.2 An Observatory Model

Each observatory can be characterized by its operating energy band, its energy dependent effective area, its event position reconstruction accuracy $\vec{\sigma}$, and its background event rates (R_B). In general, these factors combined with a source function lead to an incident event rate from the source given by:

$$R_S(t) = \frac{N}{\Delta t} = \int_{E_1}^{E_2} A_{\text{eff}}(E)\Phi(E)dE \tag{3.11}$$

where E_1 is the lower bound on the operating energy (effectively the point where $A_{\text{eff}} = 0$), E_2 is the upper bound on the operating energy, and $R_S(t)$ is the event count rate (either number of neutrinos or photons). For the neutrino observatory model, the IceCube observatory was chosen as basis for a simple "toy model". For the gamma ray observatory model, both the Fermi Large Area Telescope and the Swift Burst Alert Telescope were chosen as a basis for a "toy model".

3.2.1 Modeling Icecube

For a neutrino observatory, the 86 string and the 40 string Icecube observatory[1] in Antarctica were considered[2]. Essentially, Icecube detects neutrinos interacting in the ice sheets of Antarctica using Cherenkov flashes. IceCube has the ability to reconstruct the paths of muon neutrinos above 0.1 TeV, tau and electron neutrino showers can be detected above 10 TeV, and tau neutrinos can be distinguished from electron neutrinos above 1000 TeV. With that said, only muon neutrinos were considered in this model as they provide better position reconstruction at low energies. The effective area dependance on energy can be seen in Fig. 3.1. Effectively, Icecube is only capable of detecting neutrinos with energies above 1 TeV (10^6 MeV) - with IC-86 being more sensitive to lower energy neutrinos than IC-40 - and has an effective area sensitive to the zenith angle (significant fall off after 300 TeV) of the source (Fig.3.1 shows a zenith angle of $z = 90°$). If the spectrum is restricted such that the neutrino energies fall below $\approx$ 300 TeV, then the effective area becomes fairly independent of zenith angle for that energy range. Additionally, only up-going neutrinos (perfectly discriminated) will be considered (declination ≥ 0) due to the domination of atmospheric muons (cosmic-rays) for down-going events. With that said, the "toy model" neutrino detector is considered to have a field of view $\Omega = 2\pi$ sr centered on the north pole ($\theta = 0$).

Considering that up-going neutrinos will exhibit low statistics (with a background rate of $R_B = 10\ \text{hr}^{-1}$), the detection probability of neutrinos will fall into the Poisson statistics regime. With that said, the probability of detecting k neutrinos can be expressed by (3.12).

$$P^{(k)} = 1 - \sum_{i=0}^{k-1} \frac{\langle N \rangle^i \, e^{-\langle N \rangle}}{i!} \tag{3.12}$$

where $P^{(k)}$ is the probability of detecting k or more neutrinos, and $\langle N \rangle$ is given by $\langle N \rangle = b_\nu + s_\nu$ and corresponds to an expected number of either background or signal neutrinos, b_ν and s_ν, respectively. Given the low detection rate expected by a neutrino observatory (i.e. IceCube) compared to the average burst time $t_{90} \approx 10 - 100$ seconds (for long GRBs), a neutrino observatory would be a good candidate to act as a trigger observatory. Additionally, only a single neutrino trigger is required for a coincident analysis with other observatories (i.e. the case where $k = 1$).

Another aspect to consider in regards to event detection is that of uncertainty in position reconstruction. Luckily the the position uncertainty or point spread function (PSF) for IceCube is approximately Gaussian given by (3.13).

$$\frac{dP(\hat{x}|\hat{x}_0)}{d\Omega} = \frac{1}{2\pi\sigma^2} e^{-\frac{|\hat{x}-\hat{x}_0|^2}{2\sigma^2}} \tag{3.13}$$

where $\hat{x}$ is a variable position within the field of view Ω, $\hat{x}_0$ is the reconstructed position, and σ is

[1] Note that the following information was obtained via internal communications with the Icecube collaboration.

[2] The 40 string and 86 string variants of Icecube were different stages / experiments in the development of the observatory. The 40 string Icecube experiment ran from 2007-2008, and the 86 string Icecube experiment from 2010-2011.

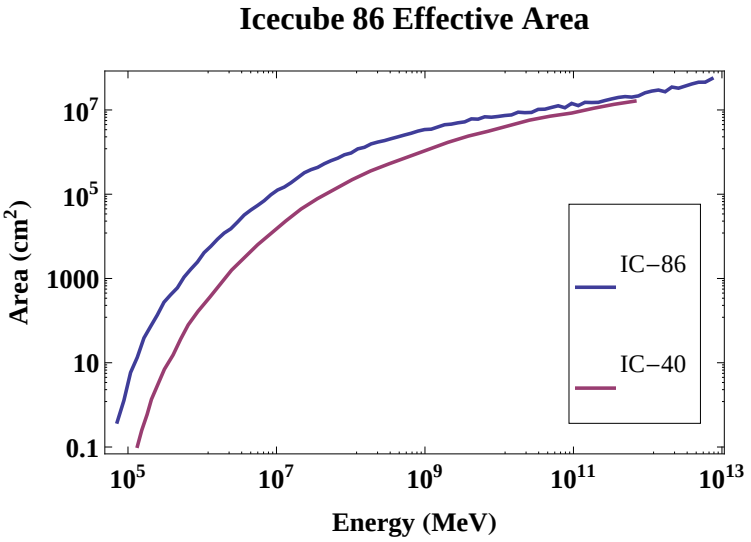

Figure 3.1: Plot comparing the Icecube 86 and Icecube 40 experiment effective areas as a function of neutrino energy for the zenith angle band of $0° - 30°$. In principle the effective area will begin to fall off to zero for larger zenith angles, however, this effect occurs at higher energies than will be considered here. Therefore, for simplicity, this effect is omitted from the model presented here.

the energy dependent. In reality, IceCube would supply a calculate σ along with a reconstructed position $\hat{x}_0$ for each event, however, an expression for $\sigma(E_\nu)$ must be obtained for modeling and simulation purposes. With that said, the energy dependent FWHM can be approximated[3] by (3.14).

$$\sigma(E_\nu) = p_0 \; E_\nu^{-p_1} + p_2 \tag{3.14}$$

where E_ν is in MeV, $\sigma(E_\nu)$ is given in radians, and the coefficients p_0, p_1, p_2 are listed in Tab. 3.1.

p_0	p_1	p_2
10.2	0.503	0.00291

Table 3.1: Table of IceCube FWHM coefficients.

[3]This expression was obtained via internal communication with a member of the IceCube collaboration after fitting real data. The form in (3.14) is the best fit to the real data.

3.2.2 Modeling Fermi-LAT

For a gamma-ray observatory, the Fermi Large Area Telescope was considered [24, 25]. Fermi LAT detects gamma-rays by using a converter material to create an electron-positron pair. The detector is then able to measure the resultant track created by the particle pair as they interact with silicon strip detectors. Additionally, photon energies are measured by using an on board calorimeter that is capable of measuring the energy dissipated by the interactions. With that said, the LAT telescope is sensitive for energies between 20 MeV and 100 GeV (See Fig.3.2), however, this gamma-ray observatory model will be considered to have sensitivity for 20 MeV and above. Similarly to Swift, the expected field of view of Fermi LAT is around 60° on either direction of the spacecraft z-axis[4].

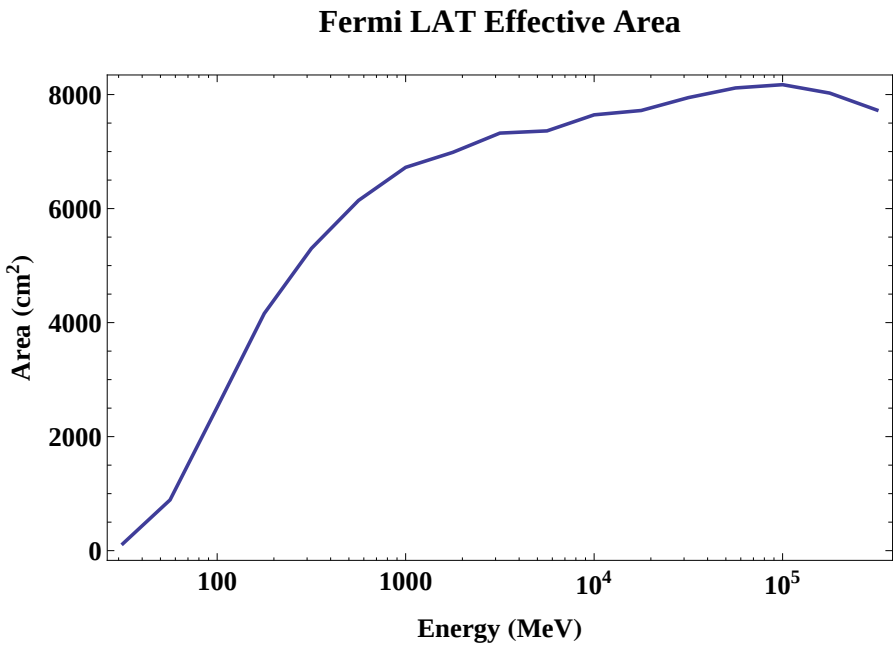

Figure 3.2: Plot of the effective area for Fermi LAT as a function of photon energy for a zenith angle near zero. Similarly to the Icecube case, the zenith angle dependence on the effective area is not considered in this model for simplicity.

Unlike the neutrino observatory example, a gamma-ray observatory (such as LAT) has a stable background rate of several thousand events per hour ($R_B \approx 2088$ hr^{-1}). This background event rate is considered to be statistically time invariant by the Fermi group, and by tests of the week 9-51 photon data sets. When comparing this large event rate to the average t_{90}, the number of expected background events resides within the Gaussian regime. Additionally, if the triggering event is a neutrino, then probability of detecting the neutrino can be neglected, and

[4]Since Fermi scans the sky, the spacecraft z-axis will swivel from a declination of approximately 30° to −30°, while the angle between the spacecraft z-axis and the earth zenith angle is non-zero.

only position reconstruction needs to be considered.

The uncertainty in the position reconstruction for LAT can be given by the a combination of King functions in (3.15).

$$\begin{aligned}
\frac{dP(\hat{x}|\hat{x}_0)}{d\Omega} &= f_c\kappa^2 K\left(\kappa|\hat{x}-\hat{x}_0|,\sigma_c,\gamma_c\right) + (1-f_c)\kappa^2 K\left(\kappa|\hat{x}-\hat{x}_0|,\sigma_t,\gamma_t\right) \qquad (3.15)\\
f_c &= \frac{1}{1+N_t(\sigma_t/\sigma_c)^2}\\
\kappa(E_\gamma) &= \left[c_0^2\left(\frac{E_\gamma}{100}\right)^{-2\beta}+c_1^2\right]^{-1/2}\\
K(z,\sigma,\gamma) &= \frac{1}{2\pi\sigma^2}\left(\frac{\gamma-1}{\gamma}\right)\left(1+\frac{1}{2\gamma}\cdot\frac{z^2}{\sigma^2}\right)^{-\gamma}
\end{aligned}$$

where E_γ is in MeV, $K(z,\sigma,\gamma)$ is the King function, and the other parameters are listed in Tab. 3.2.

N_t	σ_c	σ_t	γ_c	γ_t	c_0	c_1	β
0.08639	0.5399	1.063	2.651	2.932	5.8×10^{-2}	3.77×10^{-4}	0.80

Table 3.2: Table of parameters corresponding to the Fermi LAT point spread function given in (3.15).

Unlike Icecube, LAT expects to experience a much higher event rate, which makes reporting every photon event infeasible. While LAT does store every photon event (once they have passed through a instrumentation background rejection pass), reported "events" are aggregates of multiple photons. Here they group somewhere between 20 to 100 events given a specific time interval of $\Delta T \geq 200$ seconds[5]. The Fermi group then formulated a log likelihood function consisting of components for time and for position reconstruction as follows:

$$\begin{aligned}
\lambda &= \ln\lambda_t + \ln\lambda_p\\
\ln\lambda_t &= \sum_i \ln\left(1-\exp\left[-r_{bg}\left(t_{i+1}-t_i\right)\right]\right)\\
\ln\lambda_p &= -\max_j\left[\sum_{i\neq j}\ln P(\hat{n}_j\cdot\hat{n}_i, E_i, \theta_j)\right] \qquad (3.16)
\end{aligned}$$

where t_i is the time of the i^{th} event, r_{bg} is a time averaged background during the window, $P(\hat{n}_j\cdot\hat{n}_i, E_i, \theta_j)$ is the PSF of the instrument, $\hat{n}_i$ is the position vector of the i^{th} event, E_i is the energy of the i^{th} event, and θ_j is the angle between the candidate source direction and the spacecraft z-axis. When this analysis is performed, the LAT instrument characterizes events into two main categories: 1) Cone, and 2) psf. The cone category corresponds to events that are within

[5]The time interval is only > 200 seconds under the condition that less than 20 events were within 200 seconds, and is then extended to include the first 20 events.

17° of the spacecraft z-axis, and the psf category corresponds to everything else. By running simulations and comparing with actual data, the Fermi team has computed corresponding 5 sigma thresholds for the core and psf categories as -112 and 19, respectively [26, 27].

This sort of analysis provided by the Fermi team produces a nice clustering and rejection of background data, however, it does not report sub-threshold and weak events which are of interest to AMON. It is for this reason that individual photon events are considered in this thesis, since it is highly likely that within the set of 20 events that LAT analyzes, one of those may be signal and the other 19 be background.

3.2.3 Modeling Swift-BAT

For a second gamma-ray observatory, the Swift Burst Alert Telescope was considered [28, 29]. The BAT instrument uses an array of CdZnTe elements which continually checks for an excess of photons over a large portion of the sky. If an excess is found, the BAT instrument will formulate an "image", allowing for quick and accurate gamma-ray burst event recognition and position localization. In terms of detection of events based on energy, the BAT instrument looks in four energy bands simultaneously (See Fig. 3.3) each with their own respective background rates (See Tab. 3.3). Additionally, the BAT instrument has a field of view of 60°.

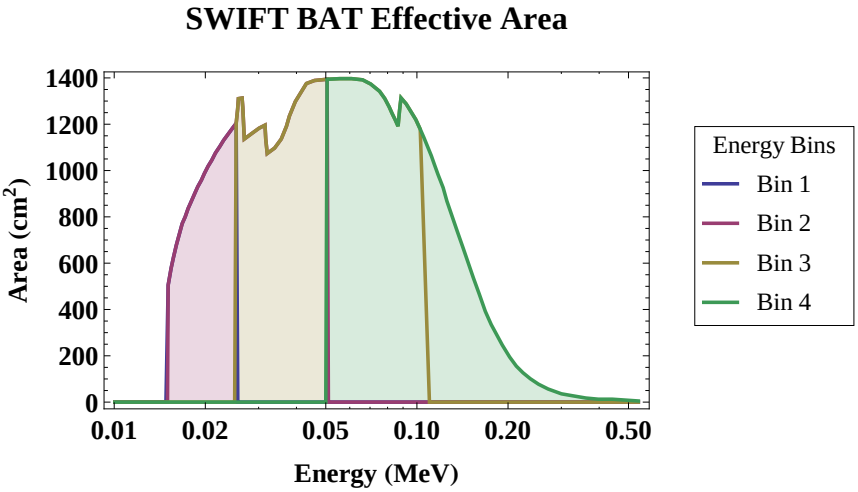

Figure 3.3: Plot of the Swift BAT effective area as a function of photon energy for the four different energy bins used by BAT. Bin 1 (blue) goes from 0.015-0.025 MeV, Bin 2 (purple) goes from 0.015-0.05 MeV, Bin 3 (yellow) goes from 0.025 - 0.1 MeV, and Bin 4 (green) goes from 0.05-0.5 MeV. These bins are shown in Table.3.3.

Essentially, BAT will continually monitor each of the four energy bins and formulate a variable S_I known as the image significance as given by (3.17). The value of S_I will be reported from each energy bin, and the largest one chosen to compare against an instrument threshold. The working threshold on BAT is set by a value of $S_I = 6.5$, which is chosen from a background

Bin	Energy Range	Background Rate
1	0.015 - 0.025 MeV	2300 Hz
2	0.015 - 0.500 MeV	4700 Hz
3	0.025 - 0.100 MeV	4700 Hz
4	0.050 - 0.500 MeV	4700 Hz

Table 3.3: Table showing the energy range as well as the average background event rate for each of the four bins shown in Fig.3.3

distribution of S_I (See Fig. 3.4). Events with both sub-threshold and above threshold values of S_I were considered, using a minimum cutoff of $S_I = 5$.

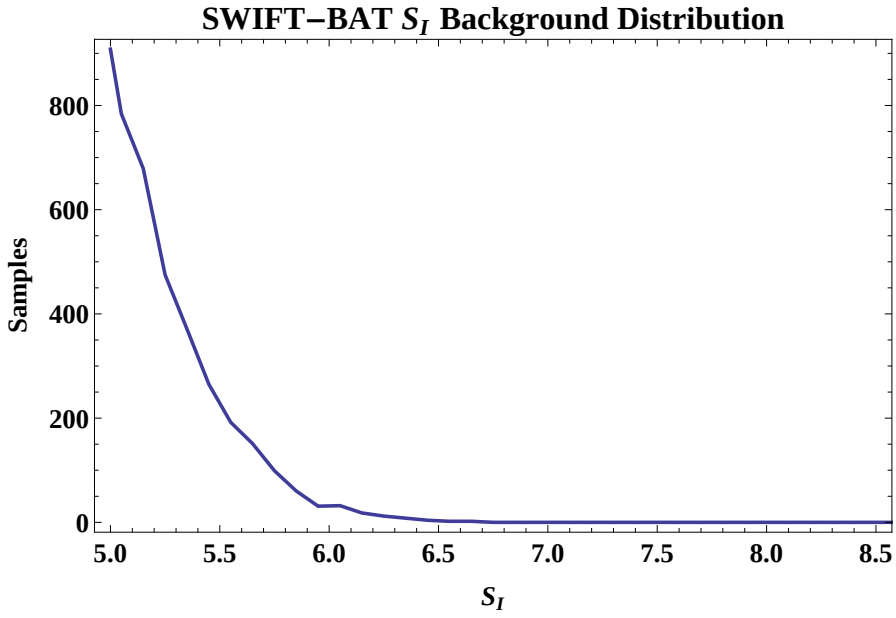

Figure 3.4: Plot showing the un-normalized background event distribution for the image significance S_I of Swift BAT. BAT defines $S_I < 6.5$ to be subthreshold, and $S_I < 5.0$ to be below detector limitations.

$$S_I = f\frac{s_\gamma}{\sqrt{s_\gamma + b_\gamma}} \tag{3.17}$$

where s_γ is the expected photon count for the given energy bin, and b_γ is the expected background count for the energy bin, and $f = 0.73$ to account for the finite size of the detector pixels.

In regards to position reconstruction error, BAT is extremely good at reconstructing position and thus its PSF in comparison with most other observatories can be considered to be a delta function centered on the reconstructed position. In reality this PSF has a spread of around 17 arcminutes, however, compared to the other observatories, it can be treated as a delta function.

Chapter 4

Monte-Carlo Results

4.1 Self-Coincident Analysis of IceCube Data

One of the first cases to look at would be the example of a currently possible analysis consisting of subthreshold neutrino doublets[1]. Since this analysis is dealing with events located on the unit sphere, spherical coordinates would be the natural choice to describe the position of an event in the sky (on the celestial sphere), and would be described with coordinates given by $\hat{x}_i = \hat{x}(\theta_i, \phi_i)$. For simplicity in the numerical simulation, the true event position of both the null and alternate hypothesis were chosen to be at the pole of the northern hemisphere[2](i.e. $\hat{x}_{actual} = \hat{x}(0,0)$). In both cases, the first neutrino event ξ_1 is considered to be a "trigger" neutrino, which can either be in coincident with a background neutrino ($\mathcal{H}_0$) or with another signal neutrino ($\mathcal{H}_1$). For the null hypothesis case, both neutrino events can be uniformly distributed over the northern hemisphere and follow an energy distribution that that goes as $\propto E_\nu^{-3.7}$ - the measured atmospheric background distribution for neutrinos.

For the signal case, the "intensity" of the source ($\langle s_\nu \rangle$ - the expected number of neutrinos) is neglected in the Monte-Carlo simulation, as the initial condition of a neutrino doublet is already imposed (i.e. $s_\nu = 2$). In the post simulation analysis, the actual intensity parameter $\langle s_\nu \rangle$ in the space Λ is separable from the Likelihood analysis. The two events considered had their energies picked from a signal like distribution. For simplicity, a signal distribution that follow $\propto E_\nu^{-2}$ was chosen as it is significantly different from the background distribution, and has a finite number fluence. The positions can be generated uniformly in the coordinate ϕ due to the degeneracy in polar coordinates for a solution at the pole, and their θ coordinate can be chosen based on the energy dependent point spread function (PSF) centered on the northern pole.

[1] IceCube currently only considerers neutrino triplets to be above threshold, and considers doublets and lower to be subthreshold.

[2] This choice was made due to the fact that IceCube has a FOV $\approx 2\pi$ in the northern hemisphere.

The log-likelihood ratio can then be formed for the case of neutrino doublets as follows:

$$\lambda = -2\left[\sum_{k=1}^{2} \ln B_{IC}(\hat{x}_k) - \sum_{k=1}^{2} \ln S_{IC}(\hat{x}_k|\hat{x}_0)\right] \tag{4.1}$$

where $\hat{x}_0$ is the best fit position, $\hat{x}_k$ is the position of the event k, S_{IC} is the signal probability distribution function (in this case the PSF), and B_{IC} is the background probability distribution (in this case a uniform PSF over the FOV of the observatory). Applying the distributions as stated above, the expression for λ reduces to:

$$\lambda = 2\left[-\frac{(\hat{x}_1 - \hat{x}_0)^2}{2\sigma_1^2} - \frac{(\hat{x}_2 - \hat{x}_0)^2}{2\sigma_2^2} - \ln(2\pi\sigma_1^2) - \ln(2\pi\sigma_2^2) + 2\ln(\Omega_{12})\right] \tag{4.2}$$

With,

$$S_{IC}(\hat{x}_k|\hat{x}_0) = -\frac{(\hat{x}_1 - \hat{x}_0)^2}{2\sigma_1^2} - \frac{(\hat{x}_2 - \hat{x}_0)^2}{2\sigma_2^2} - \ln(2\pi\sigma_1^2) - \ln(2\pi\sigma_2^2) \tag{4.3}$$

$$B_{IC}(\hat{x}_k|\hat{x}_0) = -2\ln(\Omega_{12}) \tag{4.4}$$

where σ_i is the energy dependent uncertainty in position, and Ω_{IC} is the FOV of the observatory. It can be seen that this expression has a simple analytic maximum which, assuming small angles reduces to:

$$\lambda_{fit} = -\left[\frac{\theta_{12}^2}{\sigma_q^2} + 2\ln(\sigma_q^2)\right] \tag{4.5}$$

where $\cos(\theta_{12}) = \hat{x}_1 \cdot \hat{x}_2$, and $\sigma_q^2 = \sigma_1^2 + \sigma_2^2$. As a result, the distribution for both the null and alternate hypothesis can be obtained without numerically solving a minimization problem. A Monte Carlo simulation lends itself well to solving this sort of problem by accumulating statistics by a series of trials that sample a specific event space Ξ. With that said, the resulting distributions for the null and alternate hypothesis for the case of 10^4 trials can be seen in Fig 4.1.

Both the null hypothesis distribution and the alternate hypothesis are normalized and are displayed using equal bin widths. Due to the fact that the generation of the histograms in Fig.4.1 is independent of the specific event space Ξ a general ROC curve can be generated by varying the value λ_{th}. The resultant curve can be seen in Fig.4.2 plotted along with the random guessing line. It should be noted that the ROC curve in Fig.4.2 only displays up to a false positive probability of 10^{-4}, to look at the behavior of the ROC curve below this, more statistics and thus more trials would be needed.

The next task is to interpret and make some physical sense of the ROC curve. The false alarm rate (FAR) will be directly connected to the false positive probability $P(\mathcal{F}_0)$ on the ROC curve. Specifically, the rate of false positives can be thought of as the rate of atmospheric neutrinos (the only false signal that is being considered here) combined with the probability that the atmospheric neutrinos will be detected as part of the doublet, and with the probability of the analysis accepting the doublet as actual signal. From the neutrino model proposed in the previous chapter, the FAR can be calculated as in (4.6).

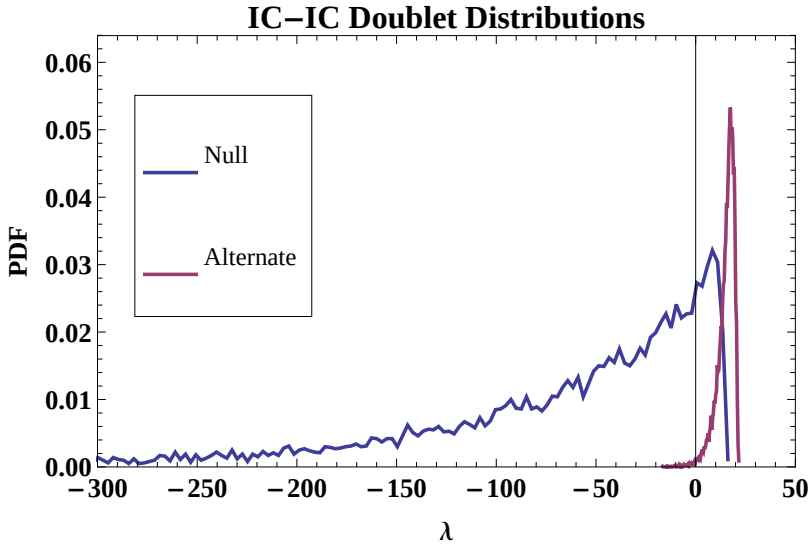

Figure 4.1: Probability distributions for the $\mathcal{H}_0$ and $\mathcal{H}_1$ cases of the IC-IC doublet analysis. Both distributions are discreetly normalized, and are scaled to use the same binning. A vertical line is drawn at the $\lambda = 0$ point in which denotes the case where $\mathcal{H}_0$ and $\mathcal{H}_1$ appear to be identical, and therefore essentially equates to the random guessing line on the ROC curve.

$$FAR = R_{atm}\left(1 - e^{-R_{atm}\Delta T\frac{\Delta\Omega}{\Omega_{IC}}}\right)P(\mathcal{F}_0) \tag{4.6}$$

where Ω_{IC} is the FOV of the observatory, $\Delta\Omega$ is a spatial cut placed on the events, and the value of ΔT is a temporal cut on the time the two neutrino events must be within to be considered a doublet. Both of the cuts (spatial and temporal) are considered to be hard box cuts[3].

To put the values of true positives $P(\mathcal{T}_1)$ in perspective of event space Ξ in Λ the actual acceptance can be considered in terms of a ratio of possible event detection on the celestial sphere multiplied by a probability of detecting two signal events to obtain a rough acceptance value. The rough value can then be multiplied by a more refined value for acceptance which in this case is $P(\mathcal{T}_1)$. This can be seen in (4.7).

$$A_{total} = \frac{\Omega_{IC}}{4\pi}\left(1 - e^{-\langle s_\nu\rangle} - e^{-\langle s_\nu\rangle}\langle s_\nu\rangle\right)P(\mathcal{T}_1) \tag{4.7}$$

where A_{total} is the total acceptance of the algorithm for a given value of $\langle s_\nu\rangle$, the fraction out front is the ratio of possible event detection on the celestial sphere, and the value of s_ν is the number of signal neutrinos detected by the detector based on an energy distribution and the effective area of the detector. The value $\langle s_\nu\rangle$ is essentially the number fluence $\mathcal{N}$ weighted by the energy dependent effective area of the detector. Another way to look at the value $\langle s_\nu\rangle$ is to consider it

[3]In practice a more gradual model (such as a bell curve) could be considered instead of the hard box cut

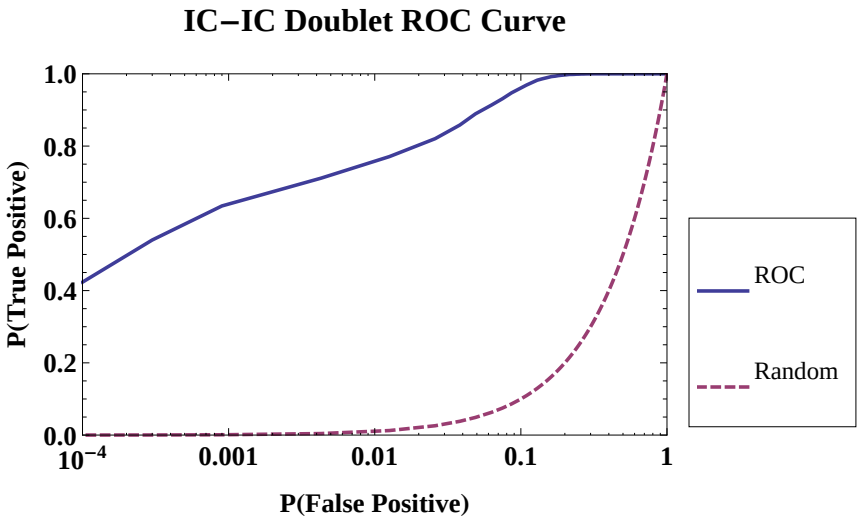

Figure 4.2: ROC curve depicting the acceptance as a function of false-positive rejection for the IC-IC doublet analysis (blue,solid). Additionally, the "random guessing" line is shown (purple,dashed), which denotes the ROC curve obtained from randomly assigning $\mathcal{H}_0$ and $\mathcal{H}_1$ to the events. To see the detail of the curves, they were plotted in Log-Linear scale.

to be the unique coordinate that identifies the event space Ξ in Λ (i.e. $\Xi = \Xi(\langle s_\nu \rangle) \in \Lambda$).

For the case of $\Delta\Omega = 0.24682$ sr (corresponding to a 17° cut - for consistency with later analysis), $\Omega_{IC} = 2\pi$ sr, $R_{atm} = 10$ hour^{-1}, $FAR = 10$ year^{-1}, and $\Delta T = 100$ s, the values of true positive and false positive become $P(\mathcal{T}_1) = 0.7744$ and $P(\mathcal{F}_0) = 0.010462$, respectively. This gives a map of the overall acceptance A_{total} as a function of the parameter $\langle s_\nu \rangle$ in Λ. The result of this map can be seen in Fig.4.3. As expected, the total acceptance tails off at a constant value for values of $\langle s_\nu \rangle \geq 2$, reaching the maximum effectiveness of the analysis, and decays to zero as $\langle s_\nu \rangle$ decreases.

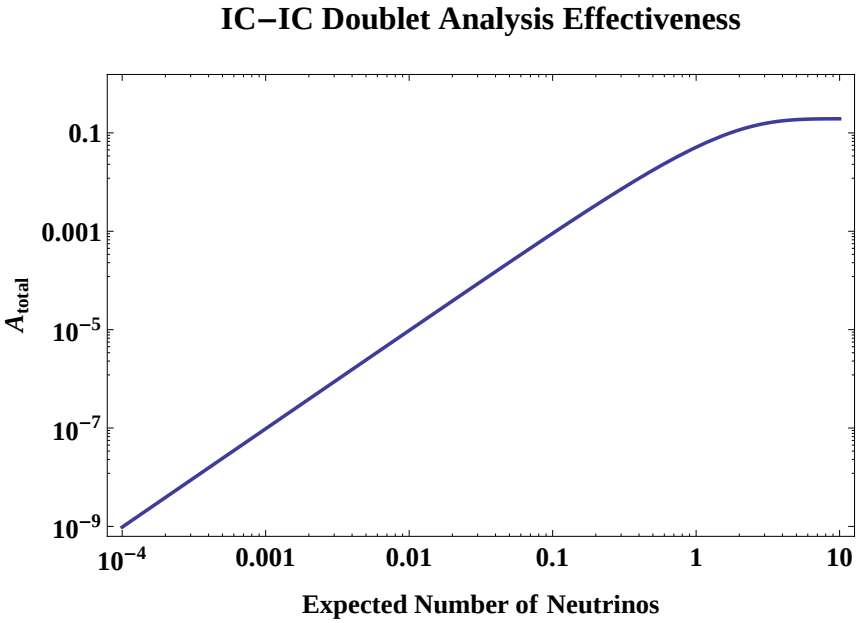

Figure 4.3: Acceptance of the IC-IC doublet analysis for different numbers of expected neutrinos s_ν. The x-axis directly correlates to the intensity of the neutrino signal via f_ν and is analogous to the photon spectral intensity parameter f_γ.

4.2 Coincident Analysis of Swift-BAT and IceCube Data

Another case to consider is that of a coincident analysis between IceCube and Swift-BAT[4]. Here a single neutrino is considered as a trigger which will look for a sub-threshold Swift-BAT event in coincidence. Much like the IceCube doublet case, position and signal "strength" can be used by the likelihood analysis, where the null hypothesis case consists of a signal strength $\langle s_\gamma \rangle = 0$ and uniformly distributed on the celestial sphere. Since the PSF for Swift-BAT is much smaller than that of IceCube, the PSF for Swift-BAT can be considered to be a delta function centered on the event reconstruction position (i.e. the true event position). For simplicity in the alternate hypothesis case, the event position can be simulated to be at the north celestial pole with $\hat{x}_{BAT} = (0, 0)$, where the IceCube neutrino has a value of θ generated from its PSF centered on the north celestial pole.

This example adds the extra complication of modeling BAT triggering for an expected number fluence of signal photons ($\langle s_\gamma \rangle$) along with a coincident analysis with an IceCube neutrino. For the triggering, the expected photon number fluence is calculated for each of the four BAT Energy bins, and compared with the background number fluence to obtain an expected value for the image significance $\langle S_I \rangle$. The bin with the largest value of $\langle S_I \rangle$ is chosen, and used for the rest of the analysis [30]. Since the background number fluence is given in terms of a rate for each bin, a triggering time of 1 second is chosen (a typical triggering time for BAT) to obtain a value for b_γ

[4]This analysis is currently done by the Icecube Collaboration, however, they only consider above threshold Swift events (i.e. $S_I > 6.5$).

and it is assumed that all of the signal γ photons are incident on the BAT detector within that triggering time window. Furthermore, Gaussian statistics can be assumed where the measured value of S_I by the instrument is Gaussian distributed around $\langle S_I \rangle$ with a FWHM given by:

$$\sigma_I = \frac{f}{2}\left(\frac{s_\gamma + 2b_\gamma}{s_\gamma + b_\gamma}\right) \tag{4.8}$$

where σ_I is the FWHM of the S_I distribution, f is the pixel scaling factor, s_γ is the expected number of signal photons, and b_γ is the expected number of background photons. It follows from this that the signal probability distribution can be expressed by:

$$S_{BAT}(S_I|\langle S_I \rangle) = \frac{1}{\sqrt{2\pi\sigma_I^2}} e^{-\frac{(S_I - \langle S_I \rangle)^2}{2\sigma_I^2}} \tag{4.9}$$

Similarly, the background probability distribution $B_{BAT}(S_I)$ can be expressed by the empirical results shown in Fig.3.4. With that, and the previous definitions for $S_{IC}(\hat{x}_k|\hat{x}_0)$ and $B_{IC}(\hat{x}_k|\hat{x}_0)$ from the previous section, the Likelihood analysis can be formed. In this case, there are two null hypothesis that must be considered: 1) Neither BAT or IceCube are detecting a signal event, 2) BAT is detecting a signal event while IceCube is detecting a background event. These two hypothesis can be combined with some parameter ϵ representing the ratio of the two possible cases. This value can be approximated as the fraction of BAT triggers that are real sources. With that said, the Likelihood analysis can be formed by:

$$\begin{aligned} \lambda = & - 2[\ln\left(S_{BAT}(S_I|\langle S_I \rangle) S_{IC}(\hat{x}_\nu|\hat{x}_{BAT})\right) - \ln\left((1-\epsilon) B_{BAT}(S_I) B_{IC}(\hat{x}_\nu)\right) \\ & - \ln\left(\epsilon S_{BAT}(S_I|\langle S_I \rangle) B_{IC}(\hat{x}_\nu)\right)] \end{aligned} \tag{4.10}$$

Similarly to the IceCube doublet case, the result for the maximum likelihood has an analytic expression given by:

$$\lambda_{fit} = -\left[\frac{\theta_{\nu\gamma}^2}{\sigma_\nu^2} + 2\ln(\sigma_\nu^2) + 2\ln\left((1-\epsilon)\sqrt{2\pi\sigma_I^2} B_{BAT}(S_I) + \epsilon\right)\right] \tag{4.11}$$

where $\theta_{\nu\gamma}$ is the opening angle between the neutrino and BAT event, σ_ν is the PSF position uncertainty for the neutrino event, σ_I is given above, and $B_{BAT}(S_I)$ is computed via a tabulated function from the histogram data in Fig.3.4. As in the IceCube doublet case, a Monte carlo simulation can be used to obtain the relevant distributions. To do so, a hardware cut must also be considered on S_I, where anything below $S_I = 5$ must be rejected as it is below the point where the BAT hardware can be considered to be reliable. For any set of events in the simulation that exhibit this characteristic, the event is culled by giving it a $\lambda_{fit} = 0$ (i.e. the signal to noise is unity where $\mathcal{H}_0$ and $\mathcal{H}_1$ are identical).

It should be noted that in this case the value of $\langle s_\gamma \rangle$ is not separable from the analysis, resulting in an inability to plot a general ROC curve. However, to get a sense of the null hypothesis

and alternate hypothesis distributions, $\langle s_\gamma \rangle = \langle b_\gamma \rangle$ was plotted in Fig.4.4, with $\langle b_\gamma \rangle = 4700$, $\epsilon = 85\text{yr}^{-1} \cdot \Delta T$, and $\Delta T = 100\text{s}$.

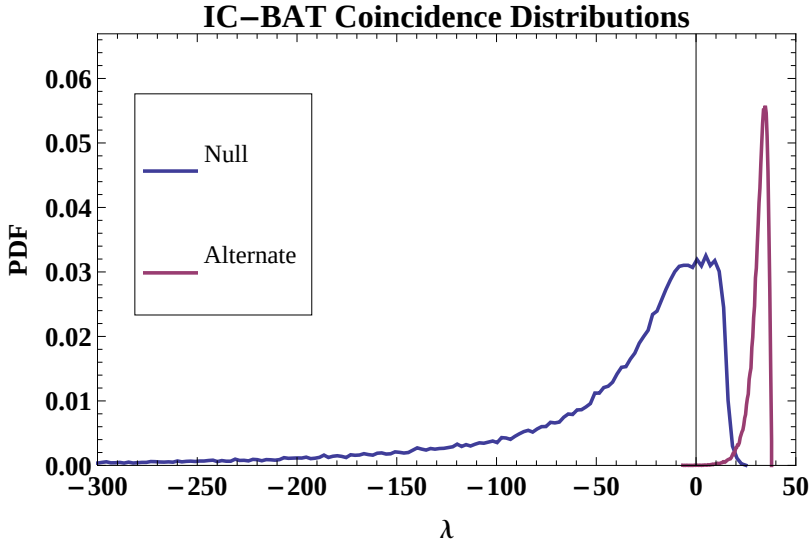

Figure 4.4: Probability distributions for the $\mathcal{H}_0$ and $\mathcal{H}_1$ cases of the IC-BAT coincident analysis, with parameters $\langle s_\gamma \rangle = \langle b_\gamma \rangle = 4700$, $\epsilon = 85\text{yr}^{-1} \cdot \Delta T$, and $\Delta T = 100\text{s}$. Both distributions are discreetly normalized, and are scaled to use the same binning. A vertical line is drawn at the $\lambda = 0$ point in which denotes the case where $\mathcal{H}_0$ and $\mathcal{H}_1$ appear to be identical, and therefore essentially equates to the random guessing line on the ROC curve.

As for making physical sense of the ROC curve generated for each value of $\langle s_\gamma \rangle$, the false alarm rate can be given by some rate of backgrounds for Swift-BAT over the FOV to obtain the background probability rate per unit solid angle. The same can be done for IceCube and be multiplied together as per combination of probabilities, followed by some multiplication of a joint FOV in solid angle Ω_{joint} (the amount of sky that IceCube and BAT jointly cover) by a solid angle $\Delta\Omega$ for the spatial coincidence cut, the triggering time cut ΔT, and finally the probability of the analysis obtaining a false positive. This is expressed in the following:

$$FAR = \left(\frac{R_{atm}}{\Omega_{IC}} \frac{R_{BAT}}{\Omega_{BAT}} \Omega_{joint} \Delta\Omega \Delta T \right) P(\mathcal{F}_0) \tag{4.12}$$

where Ω_{joint} is the joint FOV of the two observatories, $\Delta\Omega$ is the cut solid angle, and ΔT is the triggering time cut. To consider the case of the total acceptance, the rate of true positives must be weighted by the percentage of the total sky that can be seen by the joint FOV and the probability of detecting one neutrino. This reduces to the following:

$$A_{total} = \frac{\Omega_{joint}}{4\pi} \left(1 - e^{-\langle s_\nu \rangle} \right) P(\mathcal{T}_1) \tag{4.13}$$

As can be seen, the value of A_{total} in this case is dependent on both $\langle s_\nu \rangle$ and $\langle s_\gamma \rangle$ - the two

parameters that define Ξ in Λ. In principle, the total acceptance can be shown on a contour plot for a specific value of FAR with the axis of $\langle s_\nu \rangle$ and $\langle s_\gamma \rangle$. In general, however, this would not be a realistic approach to take as the expected number of photons is not a particularly insightful quantity (especially for an instrument like BAT which records spectral information), where as the expected number of neutrinos is more physical. With that said, the value of $\langle s_\gamma \rangle$ can be obtained from integrating the spectrum and finding the number fluence with a weighting of the effective area as per (3.3). By doing so, four parameters are introduced ($f_\gamma,\ \epsilon_\gamma,\ \alpha_\gamma,\ \beta_\gamma$) to replace $\langle s_\gamma \rangle$. While this is more physical, it leads to issues regarding visualization.

To begin to understand the analysis algorithm's behavior, a plot of analysis acceptance A_{total} over the parameter space denoted by $\langle s_\nu \rangle = 1$, $f_\gamma \in [10^{-3}, 10]$, $\beta_\gamma = 2.0$, $\epsilon_\gamma = 0.2\text{MeV}$, $\alpha_\gamma \in [0, 2.5]$, and $FAR = 10\text{yr}^{-1}$. Since the majority of the BAT energy bands are below the break energy, the post-break spectral index (β_γ) does not contribute much to the expected photon counts s_γ. Additionally, if the pre-break spectral index (α_γ) is large, then the expected s_γ will be larger, suggesting that events with a harder pre-break spectral index will have a higher acceptance. This data was visualized in Fig.4.5, with an added line denoting the $S_I = 6.5$ mark (i.e. the current BAT threshold).

It can be seen that the acceptance for this coincident analysis remains "large" for a substantial part of the sub-threshold event space (left of the $S_I = 6.5$ line). This indicates a potentially large advantage to this type of coincident analysis. Unfortunately BAT is less sensitive to soft pre-break spectral indices, and therefore leads to a "gap" (a region of low analysis sensitivity) in event space coverage by this analysis method.

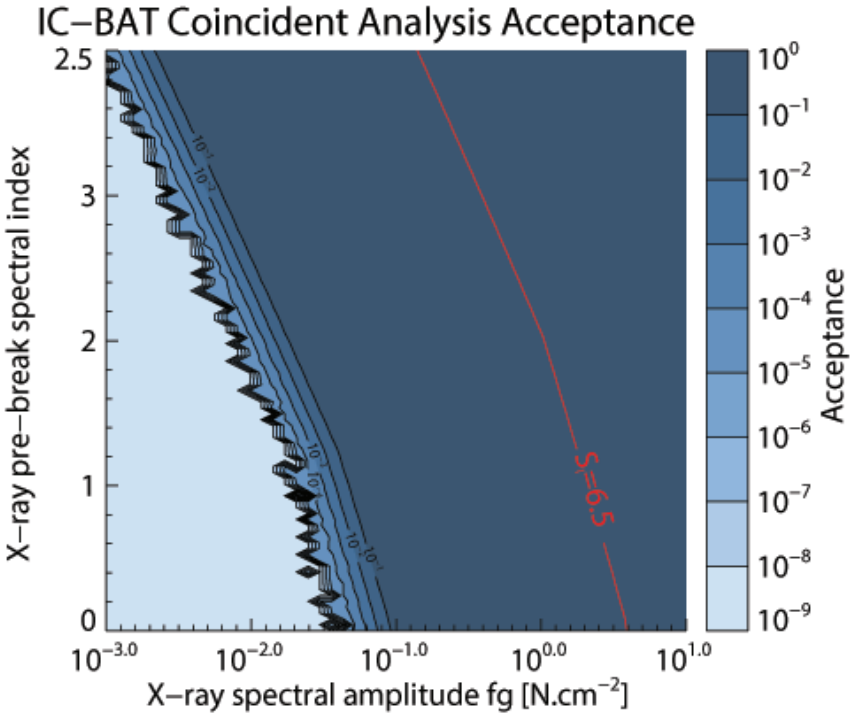

Figure 4.5: Contour plot visualizing the analysis acceptance A_{total} for the IC-BAT coincident analysis under the parameter space cuts given by: $\langle s_\nu \rangle = 1$, $f_\gamma \in [10^{-3}, 10]$, $\beta_\gamma = 2.0$, $\epsilon_\gamma = 0.2\text{MeV}$, $\alpha_\gamma \in [0, 2.5]$, and $FAR = 10\text{yr}^{-1}$. Additional plot of the BAT image significance $S_I = 6.5$ (shown in red) to indicate the current SWIFT-BAT nominal event threshold (anything to the left of the $S_I = 6.5$ line is considered "below threshold" and is therefore rejected by a stand alone BAT analysis, but remains useful to coincident analysis with a triggering observatory).

4.3 Triggered Coherent Analysis, with IceCube triggering Fermi-LAT

A third case to consider is that of an analysis between IceCube and Fermi-LAT. Since, unlike BAT, LAT is capable of detecting individual photon events (due to low background rates), two possible analysis can be considered. The first is a coincident analysis between IceCube and Fermi-LAT based on event packets from the LAT on board triggering algorithm. This case essentially becomes a coherent analysis on the LAT data coupled with a coincident analysis with the IceCube data. The term coincident here is being used to identify a pairwise analysis between two events, while a coherent analysis is being used to describe multi event analysis based on a single triggering event. Alternatively, a second analysis could be to consider a coherent analysis between multiple LAT photons and a single neutrino event. This latter case is considered in this section. It should be noted that the expected number of background and signal photons for LAT is expected to be small enough to follow Poisson counting statistics. The analysis considered

here is that of a series of LAT photon events populating a stream, being triggered by spatial and temporal coincidence with a single neutrino event.

Similar to that of the IceCube doublet case, the exact event location can be taken to be at the north celestial pole[5] for the alternate hypothesis case. Here the azimuthal position ϕ for both IceCube and LAT can be generated uniformly (due to degeneracy in ϕ) and the polar angle θ can be picked from the respective observatory PSFs. There is, however, an added complexity for dealing with individual LAT photons - background contamination. Since LAT will detect photons with a specific energy and direction, each event will either be boolean signal or background. In a Monte Carlo simulation, the number of signal events can be tuned. However, the number of background events will be dependent on statistical fluctuations. In other words, the total number of LAT events for a signal number fluence s_γ will be given by $N = s_\gamma + b_\gamma$, and therefore the signal and background events must be treated differently in the initial population. Furthermore, this adds an extra parameter to be determined - the fraction of signal photons to background photons in the LAT photon sample (i.e. the ratio of $\langle s_\gamma \rangle$ / $\langle b_\gamma \rangle$).

Once a specific $\langle s_\gamma \rangle$ is chosen, the values of s_γ and b_γ can be chosen from Poisson distributions with an expectation value of $\langle s_\gamma \rangle$ and $\langle b_\gamma \rangle$, respectively. Here $\langle b_\gamma \rangle$ is given by $R_{LAT}\Delta T$, and ΔT is the temporal cut placed on the IceCube LAT event selection, and $\langle s_\gamma \rangle$ would presumably be chosen from the number fluence of the energy spectrum.

Due to the multiple LAT events, the Likelihood analysis should account for the counting statistics probability with signal s_γ given the expected number of events N, as well as position and signal probability for each of the events. With that said, the Likelihood analysis can be formulated as follows:

$$\lambda = -2\left\{\ln\left[\frac{S_{IC}(\hat{x}_\nu|\hat{x}_0)}{B_{IC}(\hat{x}_\nu)}\right] - \langle s_\gamma \rangle + \sum_{i=1}^{N} \ln\left[1 + \frac{\langle s_\gamma \rangle}{\langle b_\gamma \rangle}\frac{S_{LAT}(\hat{x}_i|\hat{x}_0)}{B_{BAT}(\hat{x}_i)}\right]\right\} \tag{4.14}$$

where $\hat{x}_0$ is the coordinate of the (assumed unknown) true source position, $\hat{x}_\nu$ is the reconstructed neutrino event position, $\hat{x}_i$ is the i^{th} LAT photon event position, S_{IC} and B_{IC} are defined in the previous section, S_{LAT} is defined by the King function PSF as in (3.15), and B_{LAT} is defined by a uniform distribution over the unit sphere (similar to that of B_{IC}). For further simplicity, the tail section of the LAT detector can be excluded from the signal probability distribution, assuming that the majority of the photon interaction is within the core of the detector.

The next issue to tackle is finding the maximum Likelihood λ_{fit} for the above Likelihood function. Since there is no analytic solution, especially considering the fact that N is variable, the value of λ_{fit} must be found using a minimization routine for a given set of events. Additionally, since it is possible that there are multiple maxima in the global space of the entire sky, a multi-modal minimization routine should be used to find values of λ_{fit}. Don't panic and hold onto your towel, fortunately the software package MultiNest [31] can be used, and the largest value

[5]This assumes that both LAT and IceCube are co-pointing at the north celestial sphere. This assumption is unrealistic since LAT does not generally point in that declination band, however, it greatly simplifies the analysis. Realistic corrections to account for the fat the LAT and IceCube are not always co-pointing can be added by a multiplicative factor.

of λ_{fit} produced by the multi-modal analysis can be chosen to be the global λ_{fit} along with the relevant parameters of position $\hat{x}_0$ and $\langle s_\gamma \rangle$. Another possibility is to place a strict enough angular cut around the triggering neutrino, leading to only one local maximum in most cases. To handle this situation, the software package Minuit2 [32] from CERN's ROOT package can be considered as it provides a versatile way for solving multi-dimensional minimization problems.

The Monte Carlo simulation written for this problem was alternatively carried out using both MultiNest and Minuit2 via an encapsulating data structure, allowing the minimizer to be selected at run time. To get an idea what these distributions look like, both the null and alternate hypothesis distributions are plotted for the case of $\langle s_\gamma \rangle = \langle b_\gamma \rangle = 58$, for both evaluation with MultiNest and Minuit2 (see Fig.4.6).

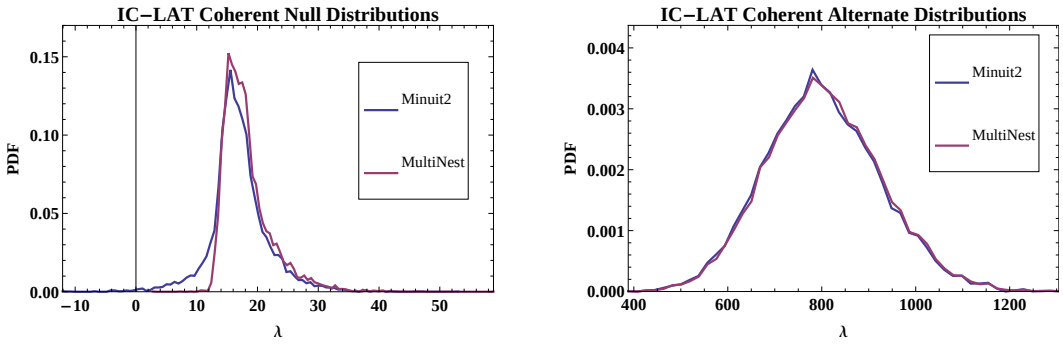

(a) Null Distributions

(b) Alternate Distributions

Figure 4.6: Plots comparing the alternate and null hypothesis distributions generated using MultiNest and Minuit2. All four distributions are normalized, and are plotted on different plots due to their relative position to one another. These distributions were produced assuming $\langle s_\gamma \rangle = \langle b_\gamma \rangle = 58$.

It can be seen in Fig.4.6 that Minuit2 and MultiNest produce very similar results for both the $\mathcal{H}_0$ and $\mathcal{H}_1$ distributions, with the $\mathcal{H}_1$ distributions being somewhat closer. For the null distributions, the two agree fairly well along the tail and begin to differ at the peak. Since in general the tail is the only aspect that really needs to be considered[6], there is no obvious statistical benefit to using one over the other. On the other hand, the Monte Carlo simulation for the alternate hypothesis case with 10^5 iterations took roughly 2 minutes to run using Minuit2, and approximately 16 hours to run using MultiNest, providing a significant computational performance gain by using Minuit2. Furthermore, fitting results (such as the covariant matrix) are more easily obtained from Minuit2 than MultiNest. Due to the nature of finding multi-modal solutions, MultiNest may be useful for realtime event stream analysis where the time required to complete a single trial would be trivial when compared to the stream event rate.

[6]If the alternate distribution passes the peak of the null distribution, the signal to noise is so poor that it might as well be assumed to be background.

4.3.1 Refined Rejection Model

Unlike in the previous two cases, the position fitting can vary greatly and resulting in a wide variety of position uncertainties (upwards of 15° depending on the spread of the initial events) due to potential spread in the LAT photon events. To deal with this issue, a secondary analysis can be considered, in which the values of λ are mapped into a new metric of D and cut on a D_{th}. This secondary analysis will allow for further rejection depending on spatial localization (how certain the reconstructed position is), and taking into consideration the field of view of the followup observatory. In fact, a weighting factor in front of the Likelihood function considering the probability of finding the sources within the FOV of the followup observatory. This translates to the following refinement to the fitted goodness parameter as follows:

$$D_{\text{fit}} = 2\ln(I) + \lambda_{\text{fit}} \tag{4.15}$$

where I is the integral over the follow up observatory's FOV of the position probability distribution centered on the reconstructed position. For this to work, the minimization routine would have to output uncertainty properties, which in this case relate to the covariance matrix of the bivariate distribution over θ and ϕ. Due to the fact that the angle mapping is non-cartesian, and there is degeneracy near the north pole, a change of coordinates can be chosen to simplify the mathematics. If small angle approximation is assumed (this has already been done in other parts of the analysis), then one can consider mapping the north pole to a cartesian grid centered with the origin in coincidence with some point near a repositioned north pole. This becomes a polar coordinate map of either (r, α) or a cartesian map of (x, y).

For this refinement, the position reconstruction was performed using a cartesian map[7] ensures that the components of the covariance matrix produced by Minuit2 are orthogonal, providing a usable result. This transformation involved using the initial distributions over θ and ϕ, followed by a map from the reconstructed neutrino location to the origin of the cartesian grid. The angles between the LAT events and the neutrino were then computed via $\hat{x}_\nu \cdot \hat{x}_i$, and mapped into the radial coordinate. The respective distributions were also modified to account for this new coordinate system.

The bivariate normal distribution is represented in (4.16) and in Fig.4.7, where σ_x and σ_y represent the variance of the distribution, and ρ represents the covariance (or skew). It should be noted that Minuit2 produces outputs for σ_x, σ_y, and ρ, which it computes internally by using the numerical Hessian matrix.

$$\begin{aligned} P(\vec{X}, \vec{\mu}, \mathbf{\Sigma}) &= \frac{1}{\sqrt{2\pi|\mathbf{\Sigma}|}} \exp\left(-\frac{1}{2}(\vec{X}-\vec{\mu})^T \mathbf{\Sigma}^{-1}(\vec{X}-\vec{\mu})\right) \\ \mathbf{\Sigma} &= \begin{pmatrix} \sigma_x^2 & \rho\sigma_x\sigma_y \\ \rho\sigma_x\sigma_y & \sigma_y^2 \end{pmatrix}, \ \vec{X} = \begin{pmatrix} x \\ y \end{pmatrix}, \ \vec{\mu} = \begin{pmatrix} x_0 \\ y_0 \end{pmatrix} \end{aligned} \tag{4.16}$$

[7] This transformation is a highly accurate approximation commonly used in Astronomy.

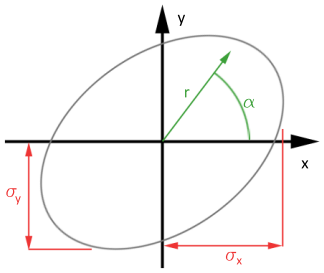

Figure 4.7: Plot of the 1σ ellipse of the bivariate normal distribution.

To compute the value of I, one must simply pull the values of σ_x, σ_y, and ρ out of the covariant matrix from the solution of the minimization library, and perform a 2-D integral over the bivariate distribution. This becomes much easier when mapped into polar coordinates, and reduces to the following expression:

$$I = \int_{r=0}^{r_{\mathrm{MAX}}} \int_{\alpha=0}^{2\pi} \frac{1}{2\pi\sigma_x\sigma_y\sqrt{1-\rho^2}} \exp\left(r^2\left[\frac{\cos^2(\alpha)}{\sigma_x^2} + \frac{\sin^2(\alpha)}{\sigma_y^2} - 2\rho\frac{\cos(\alpha)\sin(\alpha)}{\sigma_x\sigma_y}\right]\right) r dr d\alpha \tag{4.17}$$

where r_{MAX} is half of the FOV of the followup observatory. Due to the normalization, this added term is always less than one, and therefore has the effect of subtracting value from the λ_{fit} parameter by some value between $[-\infty, 0]$. A subtraction of zero ($I = 1$) would imply that the reconstructed position is very well localized within the FOV of the followup telescope, and a subtraction of $-\infty$ ($I = 0$) would imply that the reconstruction is poorly localized over the entire sky[8]. This serves the purpose of penalizing a high value of goodness if the position is poorly localized.

This followup analysis cut was performed on the previously mentioned likelihood analysis over the event space Λ using a photon spectrum model as done in the previous section. Here the break energy was taken to be $\epsilon_\gamma = 0.2$ MeV, $f_\gamma \in [10^{-5}, 10]$, $\beta_\gamma \in [1.0, 3.0]$, and the value of α_γ does not come into play here as the spectrum break is assumed to be far below the sensitivity of LAT. Additionally, a FAR of 10 yr^{-1} was chosen, with a cut angle of 17 degrees, and a followup observatory FOV of 0.4 degrees in diameter. The results can be seen in Fig.4.8. It should be noted that the followup analysis considers the probability of finding the source within one pointing of a followup observatory. This translates to an allotment of one followup pointing for every triggering event. If more pointings were to be allocated, the bivariate distribution integral I would have to be replaced with a convolution between the followup observing tilling pattern and the bivariate distribution.

It can be seen that, unlike BAT, LAT is sensitive to harder photon spectra (small values of β_γ), and therefore provides a much higher analysis acceptance for low intensity sources with harder spectra. It should be noted that the analysis acceptance contour ends at 10^{-4} due to statistical sampling issues. This sampling issue can be attributed to the initial conditions themselves which

[8]In reality since the sky is a closed surface (the surface of a sphere), the lower bound is some finite number.

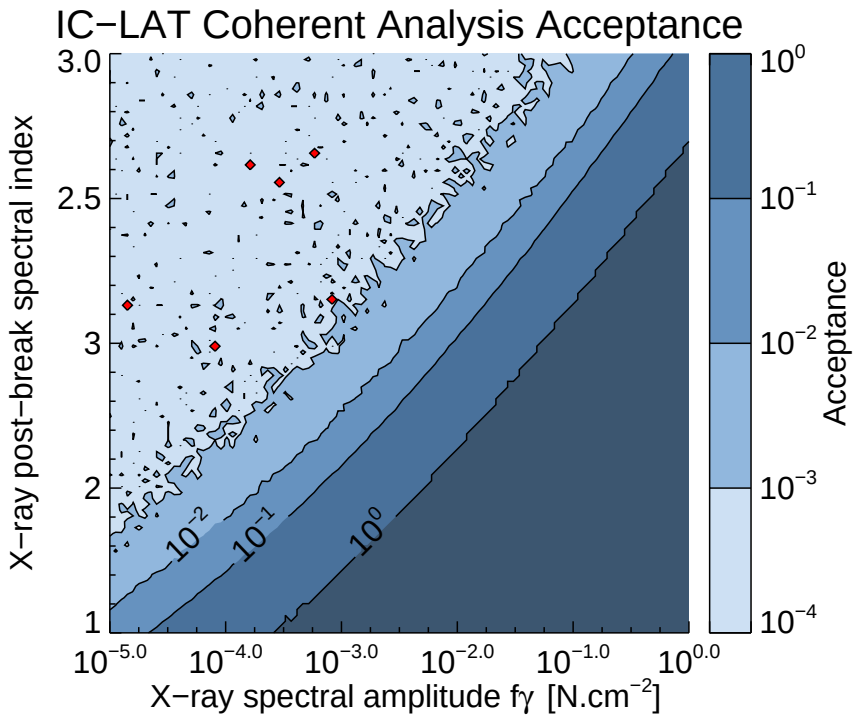

Figure 4.8: Contour plot visualizing the analysis acceptance A_{total} for the IC-LAT coherent analysis under the parameter space cuts given by: $s_\nu = 1$, $f_\gamma \in [10^{-5}, 10]$, $\epsilon_\gamma = 0.2$ MeV, $\beta_\gamma \in [1.0, 3.0]$, $FAR = 10$ yr^{-1}, $\theta_{\rm cut} = 17°$, and $FOV_{\rm Obs} = 0.4°$. It should be noted that the structures in the upper left corner are statistical fluctuations.

may produce no photons within the cut placed around the neutrino. This leads to results that must be "thrown out", yet are still counted in terms of the normalization for the distributions. As a result, instead of having 10^5 iterations, the result may be closer to 10^4 data points which place the contour limit on the lowest value being 10^{-4}.

Chapter 5

Conclusion

5.1 Discussion

It can be seen in the previous chapter that the log Likelihood analysis approach does well for weak sub-threshold signals in the presented observatory models. While a plot of analysis acceptance may be useful to demonstrate the individual analysis effectiveness over the domain of interest, it does not, however, provide an accurate way of comparing the proposed analyses to each other, or a proposed analysis to an already existing analysis (status quo). To do this, one can imagine formulating a plot which demonstrates a potential gain by dividing the new analysis acceptance by that of a status quo analysis. Furthermore, one can imagine an analysis scheme which performs all of the previously mentioned analyses (IC-IC, IC-LAT, IC-BAT) simultaneously, and allocates a certain number of follow up pointings to each of the resultant streams. To represent this, one can go about defining a gain as follows:

$$\begin{aligned} \text{Gain} &= \frac{A_{\text{ICIC}}(\lambda_1) + A_{\text{ICBAT}}(\lambda_2) + A_{\text{ICLAT}}(D_3)}{A_{\text{ICIC}}(\lambda_0)} \\ FAR_{ICIC}(\lambda_1) &= 7\ \text{yr}^{-1} \\ FAR_{ICBAT}(\lambda_2) &= 25\ \text{yr}^{-1} \\ FAR_{ICLAT}(D_3) &= 10\ \text{yr}^{-1} \\ FAR_{ICIC}(\lambda_0) &= 10\ \text{yr}^{-1} \end{aligned} \tag{5.1}$$

where the individual false alarm rates are set to reflect the number of allocated pointings for followup to each analysis. To illustrate this idea, imagine the analysis being tuned for an imaginary followup observatory with a FOV of 0.4° (this just happens to be the FOV of Swift XRT), and allows for an allocation of 70 followup pointings per year (which can be arranged in any temporal and spatial pattern). The status quo analysis would be that of an IceCube self-coincident doublet which, due to position uncertainties, would require around 7 pointings per followup in a rosette

pattern. This would translate to an allowed observatory followup false alarm rate of 10 yr^{-1} (giving a total of 70 pointings), which in turn becomes the FAR for the $A_{\mathrm{total,ICIC\ old}}$ analysis. The "new" analysis can then be considered by performing analysis on the different channels of IC-BAT, IC-IC, and IC-LAT, and have each channel share the resources of the 70 pointings. A good way to break this down would be to allocate 35 pointings to IC-IC doublet triggers (allowing for a FAR of 5 yr^{-1}), 25 pointings to IC-BAT coincidence (allowing for a FAR of 25 yr^{-1} due to the Dirac position reconstruction of BAT), and 10 pointings to IC-LAT coherent (allowing for a FAR of 10 yr^{-1})[1]. This then defines the false alarm rates for each of the pairwise triggering channels, respectively.

One complexity to consider, however, is that of the high dimensional event space, and how one could represent this gain as a function of $\gtrsim 10$ parameters. One simple way to go about doing so would be to keep several of the parameters fixed to some fiducial model. In fact there exists a "standard" model for gamma ray sources, which sets $\alpha_\gamma = 1$, $\beta_\gamma = 2$, and $\epsilon_\gamma = 0.2$ MeV. The Guetta model [16] can then be used to approximate the corresponding fiducial model for the neutrino source, setting the high energy break $\epsilon_{\nu,2} = \infty$ (which is a reasonable approximation), and decoupling the amplitudes. This would then allow for a plot that is essentially f_γ vs. f_ν, or in other words $\langle s_\gamma \rangle$ vs. $\langle s_\nu \rangle$. This gain can then also be compared to the lines corresponding to coupled amplitudes for f_γ and f_ν as a function of source isotropic luminosity for different values of the bulk lorentz factor Γ (see Fig.5.1).

It can be seen from Fig.5.1 that following up on each of the three pairwise triggering analyses sharing the same resources as a single channel analysis of IC-IC doublets, provides significant sensitivity gains. Furthermore, the combined analysis provides the most gain (10^6) in a region that has not been previously excluded as in [15], where a coincident analysis between Gamma-Ray Bursts from the Gamma-Ray Burst Network and IceCube Neutrinos (from IC-40 and IC-59) was performed using the GRB as the event trigger. No coincident events were found by [15], however, this result allowed for a 90% exclusion region to be obtained, excluding $\Gamma \lesssim 400$ (for $\epsilon_p/\epsilon_e \sim 10$). While the IceCube collaboration's analysis is different from the status quo analysis presented in this thesis (they performed a stacked analysis), comparisons can be made indicating a significant sensitivity improvement with the analysis method proposed here.

It should be noted that the gain analysis is significantly different from that of a stacked analysis in which one looks for a statistical excess. The primary difference being that the analysis presented in this thesis is to test for individual event coincidence for immediate followup, while a stacked analysis searches for a statistically significant deviation from an expected null distribution.

One can notice that the reason for the improvement lies in the requirement that the status quo analysis use two neutrinos for triggering, while the IC-BAT and IC-LAT analysis only requires one neutrino. For low rates of obtaining neutrinos (e.g. 10^{-6}) the gain ratio essentially becomes $10^{-6}/(10^{-6})^2 \sim 10^6$. With that said, it is the requirement of a single neutrino trigger, combined with an electromagnetic detection that allows for such a significant analysis gain in the excluded

[1] Here the post analysis discrimination considered the probability of finding a source within one followup FOV.

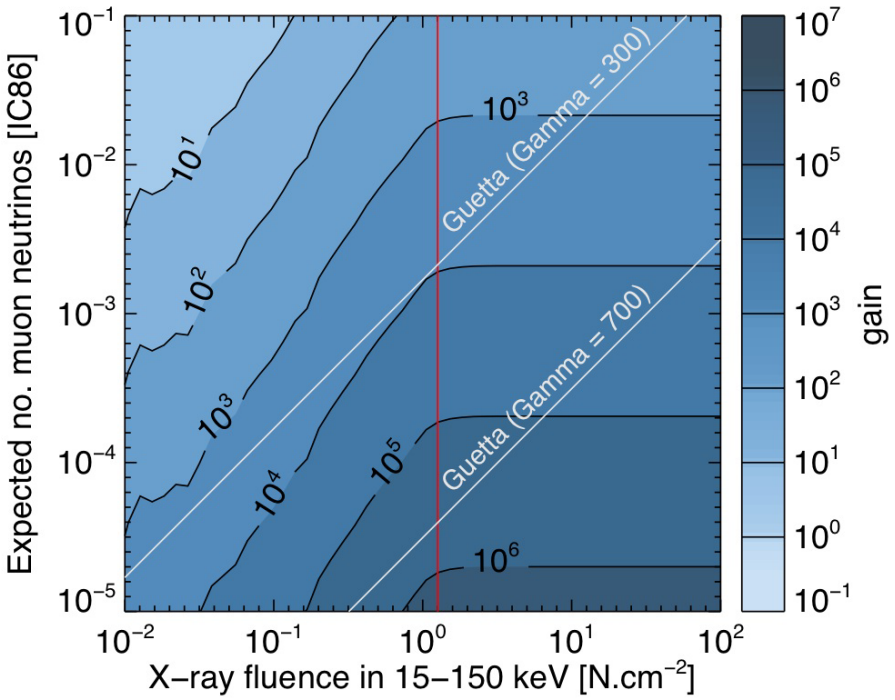

Figure 5.1: Plot comparing the combined triple channel analysis acceptance for the IC-IC, IC-LAT, and IC-BAT analysis channels sharing 70 followup pointings compared to a stand alone IC-IC analysis with 70 followup pointings. Two Guetta model lines for $\Gamma = 300$ and $\Gamma = 700$ are added to show where the combined analysis has sensitivity compare to the excluded regions (regions above $\Gamma = 300$). Additionally, the $S_I = 6.5$ line is plotted for BAT in red to divide above threshold and subthreshold events.

region and over most of the parameter space shown. There is some tapering off of the gain near high $\langle s_\nu \rangle$ and low $\langle s_\gamma \rangle$, which is due to LAT and BAT lacking sensitivity in that regime, as well as the increased likelihood of detecting a second neutrino through the status quo approach. The result becomes IC-IC/ IC-IC$\sim 0.5 \cdot 10^0 \sim 0.5$ as can be seen[2].

5.2 Future Work

The techniques presented in this thesis serve as a precursor to the eventual goal of implementing a real-time system capable of performing a multi-messenger event analysis over many observatories simultaneously. To effectively reach this goal, however, further investigation is required to understand several unanswered questions, and how they play a part in the analysis.

- Other Messenger Types: The inclusion of other messenger types such as gravity waves, neutrons (from the Galactic plane), and ultra-high energy neutrinos (EeV), could both help improve detection of events, and aid in constraining current models (e.g. a detection

[2]The 0.5 comes from the reduced allocation of resources to IC-IC neutrino doublets.

with a gravity wave can help constrain the component of gravity waves in current models). Developing a model of these additional messenger types would further inform an efficient method of multi-messenger analysis that includes these additional messenger types.

- Other Observatories: The inclusion of other observatories such as Antares(neutrinos), Hawk and Hess (gamma rays), Auger (cosmic rays), and Ligo (gravity waves), would improve the sensitivity of a multi-messenger analysis over the event space Λ. Further benefit of considering additional observatories is a greater overlap of FOV and live time between observatories allowing for the inclusion of higher multiplicity analyses.

- A More Realistic Model: The analysis presented in this thesis could be conducted using a more realistic that includes a better model for effective area ($A_{eff}(\hat{x}, E, t)$), and position reconstruction parameters ($\sigma(E, \hat{x})$, $\gamma(E, \hat{x})$, etc.). Further inclusion of a realistic FOV and live time coverage can be made between pairing observatories which do not assume always 100% coverage due to multiple co-pointing observatories. The current model could be further embellished by considering a non-uniform time-varying background ($B(E, \hat{x}, t)$), considering that the background rate on and off the Galactic plane will be significantly different in terms of amplitude and in terms of spectrum.

- Higher Multiplicity: The inclusion of more than two observatories in a single analysis could help improve multi-messenger signal detection. Doing so would allow the overall analysis parameter sensitivity to expand, as well as leverage traits that are unique to each observatory (e.g. the narrow PSF of the SWIFT BAT instrument).

- Coherent vs. Coincident Techniques: The statistical advantage to performing a coincident analysis as opposed to a coherent analysis is unknown, and should therefore be studied in more detail. An excellent example is that of a comparison of the FERMI LAT triggering algorithm, which consolidates 20 photons into a single "event" [26], as opposed to considering the 20 photon events individually as in the analysis presented in this thesis. There is an obvious computational advantage to the coincident approach, however, statistical justification is needed to recommend one method over the other. The answer to this question will help inform how to properly conduct a higher multiplicity analysis.

While the techniques presented in this thesis are based on an approximate model, they serve as an important step in understanding the statistical treatment of multi-messenger data.

Bibliography

[1] Vietri, M. and L. Stella (1998) "A Gamma-Ray Burst Model with Small Baryon Contamination," *apjl*, **507**, pp. L45–L48, astro-ph/9808355.

[2] Wang, X.-Y., S. Razzaque, and P. Mészáros (2008) "On the Origin and Survival of Ultra-High-Energy Cosmic-Ray Nuclei in Gamma-Ray Bursts and Hypernovae," *apj*, **677**, pp. 432–440, 0711.2065.

[3] Wang, X.-Y., Z. Li, E. Waxman, and P. Mészáros (2008) "Non-thermal emission from supernova shock breakout and the origin of the X-ray transient associated with SN2008D," in *American Institute of Physics Conference Series* (Y.-F. Huang, Z.-G. Dai, and B. Zhang, eds.), vol. 1065 of *American Institute of Physics Conference Series*, pp. 279–284, 0808.4006.

[4] Wang, X.-Y., S. Razzaque, P. Mészáros, and Z. G. Dai (2008) "Semi-relativistic Hypernovae as a source of UHE cosmic rays," in *American Institute of Physics Conference Series* (M. Galassi, D. Palmer, and E. Fenimore, eds.), vol. 1000 of *American Institute of Physics Conference Series*, pp. 459–462.

[5] Gao, H., W.-H. Lei, Y.-C. Zou, X.-F. Wu, and B. Zhang (2013) "A Complete Reference of the Analytical Synchrotron External Shock Models of Gamma-Ray Bursts," *ArXiv e-prints*, 1310.2181.

[6] Yu, Y.-W., B. Zhang, and H. Gao (2013) "Bright "Merger-nova" from the Remnant of a Neutron Star Binary Merger: A Signature of a Newly Born, Massive, Millisecond Magnetar," *apjl*, **776**, L40, 1308.0876.

[7] Brady, P. and S. Fairhurst (2008) "Interpreting the results of searches for gravitational waves from coalescing binaries," *Classical and Quantum Gravity*, **25**(10), pp. 105002 (26 pp.) –.

[8] Fairhurst, S. (2009) "Triangulation of gravitational wave sources with a network of detectors," *New Journal of Physics*, **11**.

[9] Pe'Er, A., K. Murase, and P. Mészáros (2009) "Radio-quiet active galactic nuclei as possible sources of ultrahigh-energy cosmic rays," *prd*, **80**(12), 123018, 0911.1776.

[10] Alvarez-Muñiz, J. and P. Mészáros (2004) "High energy neutrinos from radio-quiet active galactic nuclei," *prd*, **70**(12), 123001, astro-ph/0409034.

[11] Halzen, F., E. Zas, J. H. MacGibbon, and T. C. Weekes (1991) "Gamma rays and energetic particles from primordial black holes," *nature*, **353**, pp. 807–815.

[12] Halzen, F., B. Keszthelyi, and E. Zas (1995) "Neutrinos from primordial black holes," *prd*, **52**, pp. 3239–3247, hep-ph/9502268.

[13] Heckler, A. F. (1997) "Calculation of the Emergent Spectrum and Observation of Primordial Black Holes," *Physical Review Letters*, **78**, pp. 3430–3433, astro-ph/9702027.

[14] Ahlers, M. and F. Halzen (2012) "Minimal cosmogenic neutrinos," *prd*, **86**(8), 083010, 1208.4181.

[15] Abbasi, R. and Icecube Collaboration (2012) "An absence of neutrinos associated with cosmic-ray acceleration in γ-ray bursts," *Nature*, **484**(351).

[16] Guetta, D., D. Hooper, J. Alvarez-Muniz, F. Halzen, and E. Reuveni (2004) "Neutrinos from individual gamma-ray bursts in the BATSE catalog," *Astroparticle Physics*, **20**(4), pp. 429 – 55.

[17] Achterberg, A., M. Ackermann, J. Adams, J. Ahrens, K. Andeen, J. Auffenberg, J. N. Bahcall, X. Bai, B. Baret, S. W. Barwick, and et al. (2008) "The Search for Muon Neutrinos from Northern Hemisphere Gamma-Ray Bursts with AMANDA," *apj*, **674**, pp. 357–370, 0705.1186.

[18] Abbasi, R. and Icecube Collaboration (2010) "Search for muon neutrinos from gamma-ray bursts with the IceCube neutrino telescope," *Astrophysical Journal*, **710**(1), pp. 346 – 59.

[19] Smith, M. W. E. and AMON Collaboration (2013) "The Astrophysical Multimessenger Observatory Network (AMON)," *Astroparticle Physics*, **45**, pp. 56–70, 1211.5602.

[20] Wojtek J. Krzanowski, D. J. H. (2009) *ROC Curves for Continuous Data*, Chapman and Hall/CRC.

[21] Braun, J., J. Dumm, F. De Palma, C. Finley, A. Karle, and T. Montaruli (2008) "Methods for point source analysis in high energy neutrino telescopes," *Astroparticle Physics*, **29**(4), pp. 299 – 305.

[22] Barr, G. D., T. K. Gaisser, P. Lipari, S. Robbins, and T. Stanev (2004) "Three-dimensional calculation of atmospheric neutrinos," *prd*, **70**(2), 023006, astro-ph/0403630.

[23] Abdo, A. A., Ackermann, and Fermi LAT Collaboration (2010) "Spectrum of the Isotropic Diffuse Gamma-Ray Emission Derived from First-Year Fermi Large Area Telescope Data," *Physical Review Letters*, **104**(10), 101101, 1002.3603.

[24] Mattox, J., P. F. Michelson, P. L. Nolan, T. D. Willis, Y. C. Lin, B. Jones, B. Tompkins, B. Twiggs, M. Yearian, E. D. Bloom, W. B. Atwood, G. L. Godfrey, A. Luebke, K. S. Wood, W. N. Johnson, J. E. Grove, P. L. Hertz, M. Lovellette, D. Suson, M. Oreglia, R. Ong, H. A. Mayer-Hasselwander, M. Merk, J. D. Scargle, A. Colavita, G. Barbiellini, A. Moreselli, A. Vacchi, T. Kamae, K. Kasahara, G. Nakano, T. Burnett, R. Johnson, and L. R. Cominsky (1996) "GLAST: the Gamma Ray Large Area Space Telescope," *memsai*, **67**, p. 607.

[25] Ackermann, M. and the Fermi Collaboration (2012) "The Fermi Large Area Telescope On Orbit: Event Classifcation,Instrument Response Functions, and Calibration," *AstroPh.*

[26] Chiang, J. (2007) "LAT automated science processing for gamma-ray bursts," *AIP Conference Proceedings*, **906**(1), pp. 11 – 17.

[27] Bonnell, J. T. and J. P. Norris (2004) "GRB Trigger and Localization Algorithms Applied to GLAST Data Challenge One," .

[28] Band, D. L. (2006) "Post-Launch Analysis of Swifts Gamma-Ray Burst Detection Sensitivity," .

[29] Barthelmy, S. D., L. M. Barbier, J. R. Cummings, E. E. Fenimore, N. Gehrels, D. Hullinger, H. A. Krimm, C. B. Markwardt, D. M. Palmer, A. Parsons, G. Sato, M. Suzuki, T. Takahashi, M. Tashiro, and J. Tueller (2005) "The Burst Alert Telescope (BAT) on the SWIFT Midex Mission," *ssr*, **120**, pp. 143–164, astro-ph/0507410.

[30] Band, D., J. Matteson, and Swift Collaboration (1993) "BATSE observations of gamma-ray burst spectra. I. Spectral diversity," *Astrophysical Journal*, **413**(1), pp. 281 – 92.

[31] Feroz, F., M. P. Hobson, and M. Bridges (2009) "MULTINEST: an efficient and robust Bayesian inference tool for cosmology and particle physics," *mnras*, **398**, pp. 1601–1614, 0809.3437.

[32] James, F. and M. Roos (1975) "Minuit - a system for function minimization and analysis of the parameter errors and correlations," *Computer Physics Communications*, **10**, pp. 343–367.

Academic Vita

JOSHUA FIXELLE

Joshua Fixelle
14 Camelot Dr.
East Brunswick, NJ, 08816
jfixelle@gmail.com

Education:

Bachelor of Science Degree in Engineering Science and
Astronomy & Astrophysics, Penn State University, Fall 2013
Minors in Engineering Mechanics, Mathematics, and Physics
Honors in Engineering Science and Astronomy & Astrophysics
Thesis Title: Sensitivity Study Of Coherent Multi-Messenger Astrophysical Event Analysis
Thesis Supervisor: Miles W. Smith
Thesis Coadviser: David J. Miller

Related Experience:

Internship with Search for Extraterrestrial Intelligence (SETI)
Topic: RFI classification and discrimination with SonATA
Supervisor: Dr. Gerry Harp
Summer 2011

Publications:

Smith, M. W. E., D. B. Fox, D. F. Cowen, et al. (2012) The Astrophysical Multimessenger Observatory Network (AMON), *Astroparticle Physics,* 45.

Colas, F., J. Berthier, F. Vachier, et al. (2012) Shape and Size of (90) ANTIOPE Derived from an Exceptional Stellar Occultation on July 19, 2011, *LPI Contributions*, 1667, 6427.

Fixelle, J., & Kagan, M. (2010, November). In Haiduke Sarafian (Chair). *On deflection of potentially dangerous asteroids.* Presentation delivered and abstract published in proceedings Smith symposium 2010, York, PA.

Fixelle, J., & Johnson, K. A. (2010). Longitudinal light clock and zenos paradox. *American Journal of Undergraduate Research,* 9(2 & 3), 13-16.

Awards:

Evan Pugh Award
Spark's Award
Presidents Freshman Award
Dean's List

Presentations/Activities:

Smith Symposium Fall 2010
President of the Applied Physics Club